

The volcano-tectonic crisis of 2018 east of Mayotte, Comoros islands

Anne Lemoine^{1*}, Didier Bertil¹, Agathe Roullé¹, Pierre Briole²

¹BRGM, Orléans, France

²UMR 8538 CNRS - Ecole Normale Supérieure - PSL Research University, France

Corresponding author: a.lemoine@brgm.fr

Key words: Indian Ocean, seismic swarm, volcano seismology, deformation observation, magma migration

Key Points:

- In May 2018 a seismic crisis started offshore, east of Mayotte, Comoros islands, including the largest event ever recorded in the Comoros.
- The crisis was originally monitored with a sparse network of local accelerometers and regional broad-band stations that was gradually completed.
- Although no magma emissions was observed directly, the volcanic nature of the crisis is supported by the displacements patterns of the permanent GNSS stations of Mayotte and by the occurrence of episodic low frequency tremors.
- We present a model to interpret, at the first order, the spatiotemporal evolution of the seismological and geodetic data during the first six months of the crisis.
- The seismological and geodetic data allow to discriminate and characterize the initial fracturing phase, the phase of magma intrusion from depth to the sub-surface, and the eruptive phase that starts in early July, fifty days after the first seismic events.
- The inferred deflation source is at a depth of 28 km, and the volume involved during the first six months is larger than 1 km³. In terms of volume and depth of the source, this might be the largest off-shore volcanic event ever documented.

SUMMARY

On 2018 May 10, a seismic crisis started ~50 km east of Mayotte, the easternmost of the Comoros volcanic islands. Here we analyze its first six months, from 2018 May 10 to November 14. In that period, 29 earthquakes with magnitude greater than 5 occurred, the main one reaching $M_w = 5.9$ on 2018 May 15. In mid November, the crisis was continuing with the persistence of an unusual seismicity including episodic tremors and steady anomalous velocities measured by GNSS. The seismicity shows three successive clusters, overlapping in time and space. The coordinates of the GNSS stations also evolve in three phases, with moderate deformation during two weeks at the beginning of the crisis, quiescence from early June to early July, and the main deformation phase starting around July 10. While models of seismic dislocation cannot fit the GNSS motions, a model of deflation of magma reservoir buried in a homogenous half space fits them very well. From mid of July the deformation is steady and strong with the whole Mayotte drifting at 16 ± 1 mm/month towards east and subsiding globally at 9 ± 1 mm/month. The deflating magma chamber inferred by the model is located 45 ± 5 km east of Mayotte, at a depth of 28 ± 3 km. The rate of magma release is $82 \text{ m}^3 \text{ s}^{-1}$ which means more than 1 km^3 emitted during the first six months of the crisis. The magma might have reached the seafloor at a single point, producing a new seamount (there are others visible in the bathymetry offshore Mayotte) or along of volcanic fissure. Yet, due to the sediments thickness around Mayotte, the magma might not have reached the seafloor but instead have flown at the base of the sediments. Because of the pressure of the water (2 to 3 km depth) in the eruption area, the volcanic gasses remain in the magma. More observations at sea and seafloor in the near field are needed to constrain the characteristics of this event which could be the major submarine eruption ever documented quantitatively.

1. INTRODUCTION

On 2018 May 10, a seismic crisis started ~50 km east of Mayotte, the easternmost of the Comoros islands (Fig. 1). Several earthquakes were felt strongly by the inhabitants of Mayotte who were not specifically prepared to such hazard as the island is usually associated to moderate seismicity. We report 29 earthquakes of magnitude greater than 5, the main one reaching $M_w = 5.9$ on 2018 May 15. At the date of this paper, nine months after the start of the crisis, unusual seismicity persists with a large number of small earthquakes, episodic tremors, and the persistence of anomalous ground motion measured by Global navigation satellite system (GNSS).

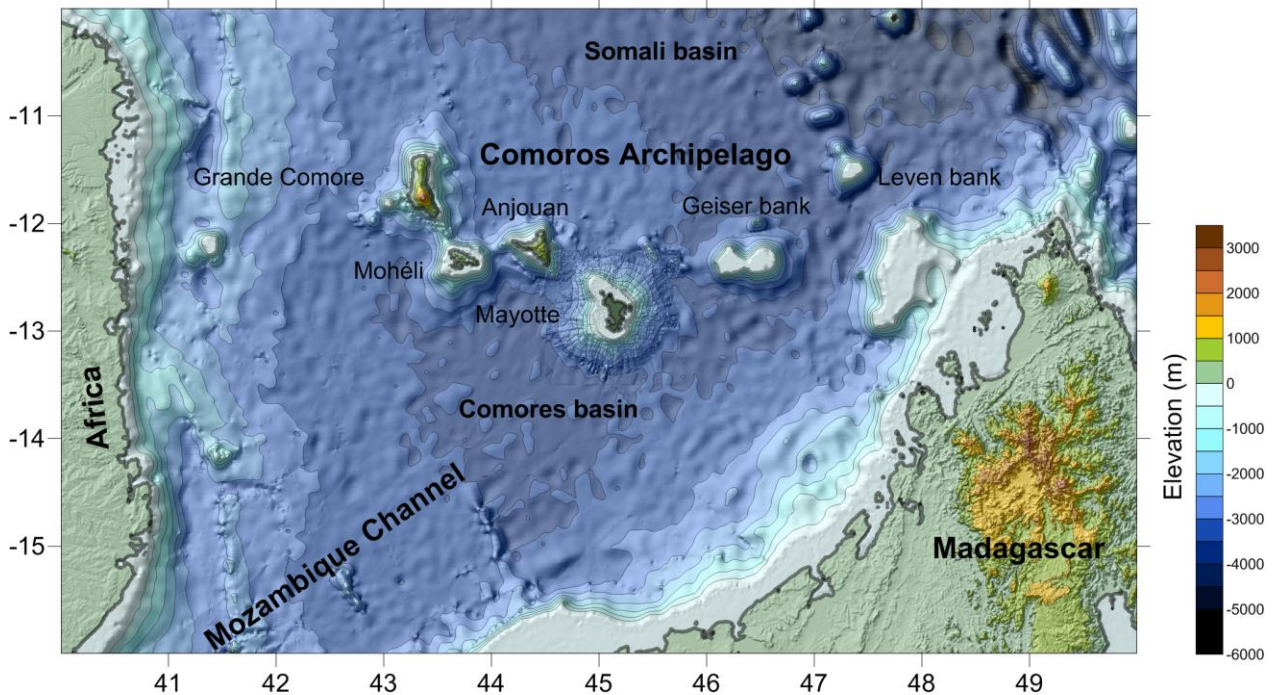


Figure 1. The Comoros islands. The Somali and Comoros basins are located north and south of the islands. Bathymetry from Gebco_2014 (Weatherall *et al.* 2015) completed around Mayotte by SHOM (2015) data.

The Comoros (Fig. 1) form a volcanic archipelago composed of four main islands, from west to east Grande Comore, Mohéli, Anjouan and Mayotte, and further east the Geiser and Leven volcanic banks (Daniel *et al.* 1972). The volcanism is younger than the Mesozoic opening of the Mozambique Channel and synchronous with the volcanism in Madagascar and the east African rift. According to rock geochronology (e.g. Nouguier *et al.* 1986, Debeuf 2004, Pelleter *et al.* 2014), the youngest volcanic activity is in Grande Comore (0.13 ± 0.02 My to present) with the active Karthala volcano, and the oldest in Mayotte (~11 My), whereas similar age is reported in Anjouan. In Mayotte Debeuf (2004) and Nehlig (2013) identify three eruptive phases separated by quiescence periods. According to Zinke *et al.* (2003a, 2003b), the latest events occurred between 4 and 7 ky in Petite Terre, northeast of the main island, where emission spots of mantellic gas still exist today (Debeuf 2004). The volcanism could be due to the presence of a hot spot, as suggested by the westward trending age (e.g. Emerick & Duncan 1982), or to

lithospheric fractures as proposed by Nougier *et al.* (1986). Debeuf (2004) proposes that an atypical hot spot is interacting with regional extensive tectonics.

2. GEODYNAMICS

The NE-SW extension across the line formed by the Comoros islands is revealed by GNSS (Fig. 2) and by the earthquake focal mechanisms (Fig. 3) (Calais *et al.* 2006; Déprez *et al.* 2013; Delvaux & Barth 2010; Stamps *et al.* 2018). Several branches of the East African rift form a distributed plate boundary zone between the Nubia and Somalia plates where Saria *et al.* (2014) defined three micro plates: the Victoria, Rovuma and Lwandle blocks. In its eastern branch, the rift continues offshore (Mougenot *et al.* 1986).

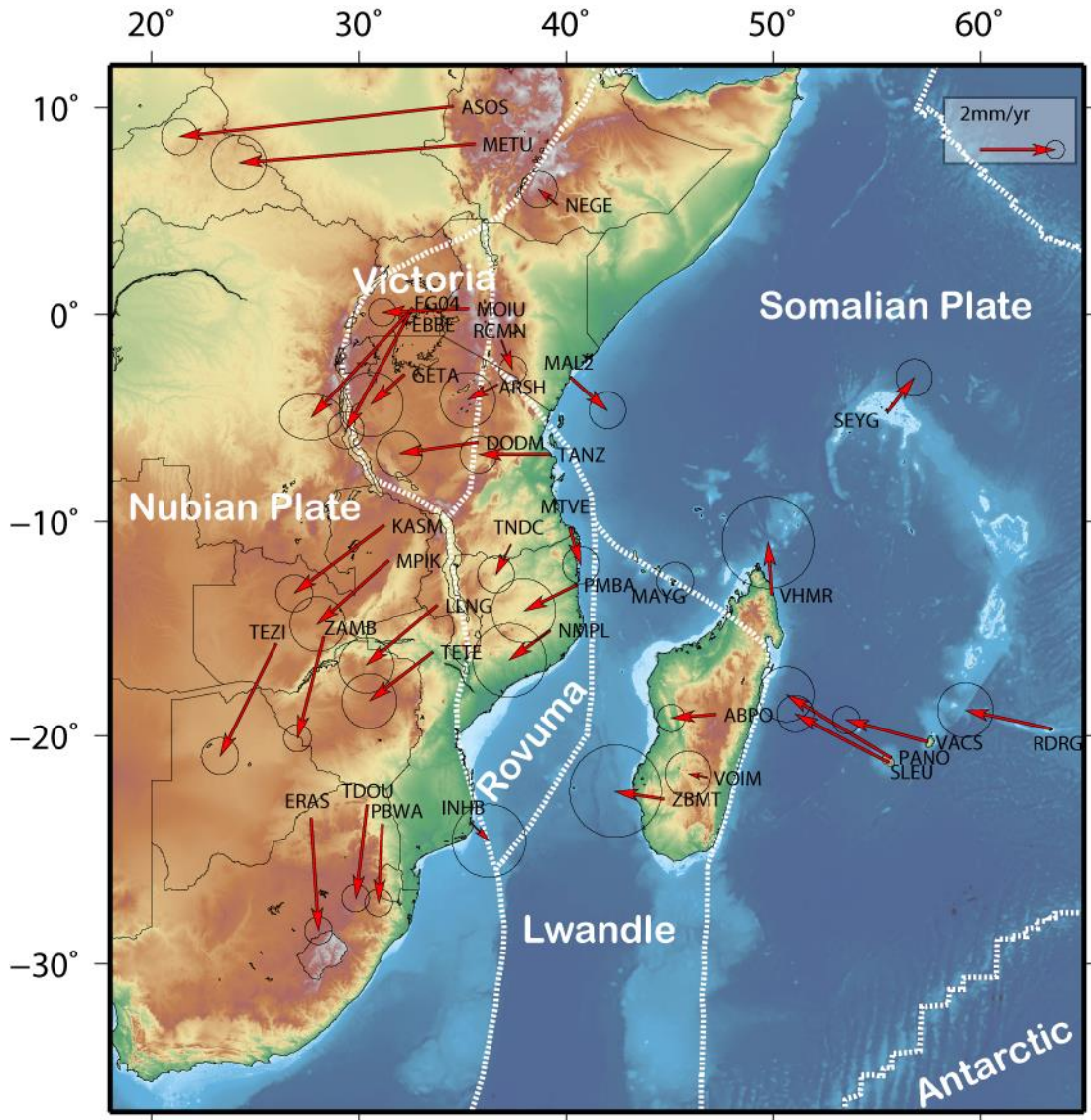


Figure 2. Map of the velocities of thirty-six GNSS stations around Mayotte (set to zero) from the time series published by the Nevada geodetic laboratory (Blewitt *et al.* 2018). The values are in Appendix 1. A clockwise correction of $2.1^\circ \text{ Myr}^{-1}$ was applied to cancel the overall rotation

around Mayotte. The plate boundaries in white dashed lines are modified from Saria *et al.* (2014) and Stamps *et al.* (2018). Elevation grid from Gebco_2014.

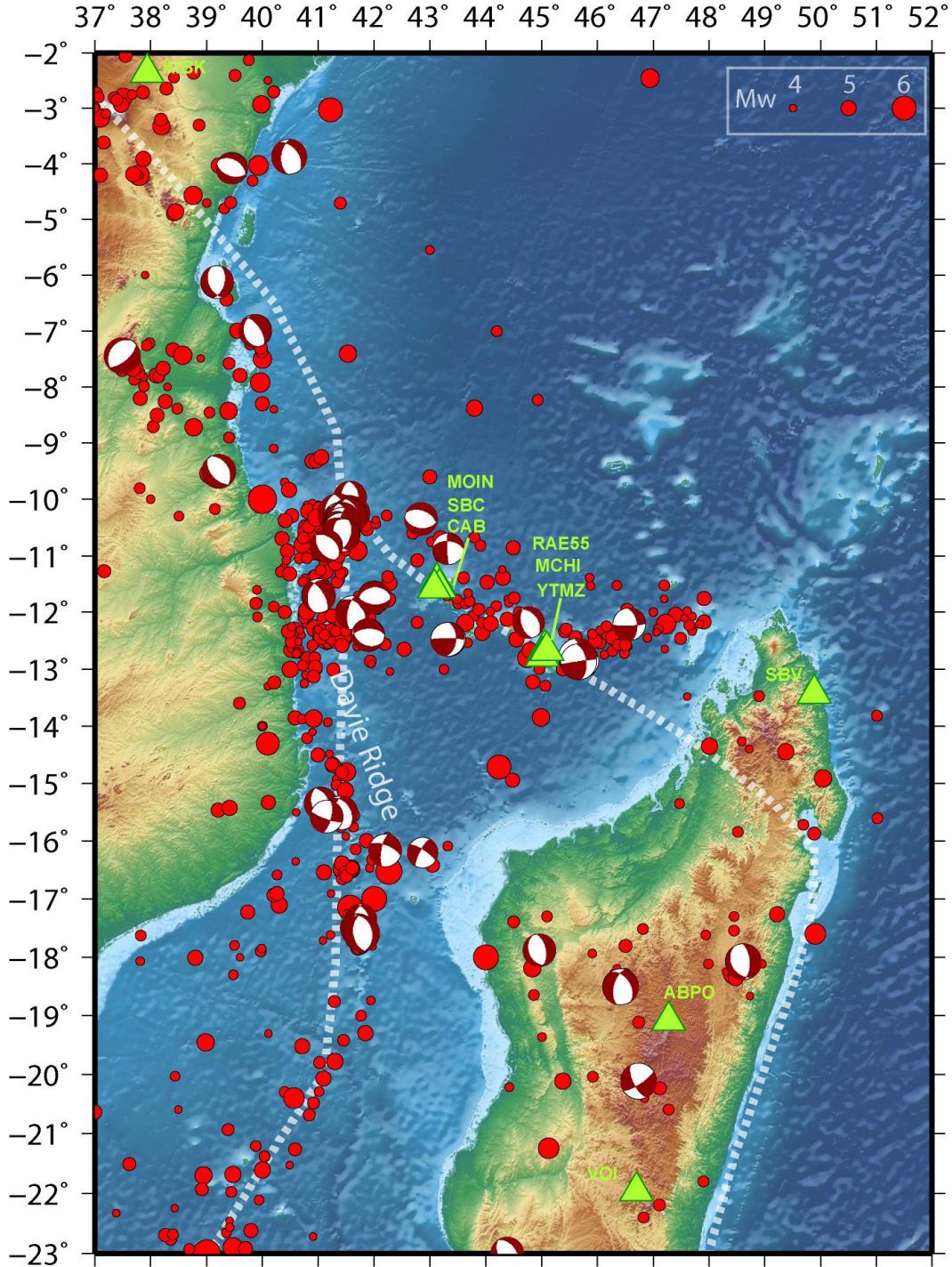


Figure 3. The 1901-2018 seismicity of $M > 4$ is merging the International seismological centre (ISC, 2016) catalogue and regional catalogue (Bertil & Regnault 1998, Bertil *et al.*, 2018). The focal mechanisms 1976-2019 are from the Global centroid moment tensor catalogue (G-CMT, Dziewonski *et al.* 1981; Ekström *et al.* 2012). The plate boundaries represented by white dashed lines are modified from Saria *et al.* (2014) and Stamps *et al.* (2018). The bathymetry and

topography are from Gebco_2014. Green triangles show the location of the seismic stations forming our monitoring network.

The boundaries of the Lwandle block are poorly constrained, especially with Somalia, and possibly diffuse (Horner-Johnston *et al.* 2007; DeMets *et al.* 2010; Saria *et al.* 2014). GNSS (Fig. 2) shows that the south of the Davie ridge is dominated by left lateral shear at a rate of 1 mm yr⁻¹ according to the difference of velocities between PMBA and NMPL on the Rovuma plate and ABPO, VOIM and ZMBT on the Lwandle plate. North of 19°S where the ridge is bending, both GNSS and the focal mechanism of earthquakes indicate the existence of extension. Strike slip events, consistent with the regional extension, exist W and SSE of the Comoros, most of them located south of the main volcanic line. The extension rate between PMBA and NMPL in Mozambique and SEYG in the Seychelles is of 2.6 ± 0.5 mm yr⁻¹ in the azimuth N50°. Part of it is accommodated across the volcanic line of the Comoros.

Whereas seismic areas and volcanism could be associated to lithospheric deformation interacting with inherited structures, and potentially associated east African rift, as Comoros coincide with its eastern border (Michon 2016). Debeuf (2004) discussed the influence of the Aswa fracture zone (east Africa), a precambrian lineament of lithospheric dimension that, despite its age, could have localized the ascent of asthenospheric plumes in the recent millions years. The location of the faulting, seismicity and volcanism could be linked to inherited crustal structures, oriented N to N320° according to Nougier (1986). Klimke *et al.* (2016) show that the tectonic history of the Mozambique Channel includes various phases of rifting, breakup Africa-Madagascar, drift of Madagascar until ~127 My, oceanic spreading in the west Somali and Mozambique basins, shear along the Davie Ridge (Ségoufin & Patriat 1981; Rabinowitz *et al.* 1983; Malod *et al.* 1991; Davis *et al.* 2016), and the development of the East African rift. Nature of substratum surrounding Comoros islands is still discussed: for example a continental origin is proposed (e.g. Flower & Strong 1969), whereas Rabinowitz *et al.* (1983) shows that most of the east Comoros basin is associated to Jurassic Magnetic Quiet Zone, so to ancient oceanic seafloor. Nehlig *et al.* (2013), suggest that the Comoros islands are lying on Comoros basin old oceanic crust, located between continental crust of Africa and Madagascar and deformed by NE-SW plio-quaternary extension. Some inherited regional structures are mapped by bathymetry and magnetic surveys, especially in the Somali basin, with E-W trending ancient ridge segments and N10°E trending transform structures according to Malod *et al.* (1991). To the south, between the Davie ridge and Madagascar, NNW-SSE fractures are reported by Ségoufin (1981), Maugé *et al.* (1982), Nougier *et al.* (1986), extending inland Madagascar.

3. THE SEISMIC CRISIS OF 2018

There are few testimonies of historical seismicity in the Comoros before the 20th century, e.g. Lambert (1997) and Sisfrance Océan Indien (2010). From 1910 to 1960, the Malagasy academy published a catalogue of locally felt earthquakes made by the Tananarive observatory. The 1936 January 16 earthquake, west of Mayotte, was felt in the whole Comoros, causing moderate damages in several municipalities (La Dépêche de Madagascar, 19/02/1936, BNF). Moderate damages are also reported for the December 1, 1993 earthquakes in Mayotte ($m_b = 5.2$).

For the period 1964-2018, we extracted a catalogue of instrumental seismicity of the Comoros from the International Seismological Center (ISC) catalogue. For 1978-1995 it was completed by

the Malagasy catalogue (Bertil & Regnault 1998), which lowers the detection threshold to $m_b = 4.0$ to 4.5 . The location accuracy is coarse, up to 30 km for many events. A band of diffuse seismicity, ~ 100 km wide, runs E-W from 48°E and 42.5°E along the volcanic line (Fig. 3). From 1982 to 2016, eight moderate earthquakes occurred (M_w 5.0 to 5.3), spread throughout this band. The last significant event close to Mayotte was an $m_b = 5.2$ earthquake on 1993 December 1.

The 2018 seismic crisis is the first long lasting crisis reported in the instrumental catalogue of the Comoros or by testimonies. When it started, the monitoring network was gathering four stations only: the accelerometer YTMZ from the French RAP network (<http://rap.resif.fr>) in Mayotte, ~ 50 km west of the crisis (Fig. 3), and, at more than 650 km, the broad-band stations ABPO and VOI in Madagascar and KIBK in Kenya from the GEOFON (GEOFON Data Centre, 1993) and IRIS/IDA (Scripps Institution of Oceanography, 1986) global networks. Late May, three broad-band stations in Grande Comore, 280 km WNW of Mayotte (Fig. 3) hosted by the Khartala volcano observatory were integrated to the monitoring network thanks to the Institut de Physique du Globe de Paris. On June 27, three stations were added in Mayotte: a broadband station from Edusismo and two RaspberryShake installed by the Bureau central sismologique français (Bcsf). Although not improving the coverage in azimuth or range, they contribute to lowering the detection threshold. Finally, on July 15, the SBV GEOFON broadband station, north of Madagascar, 450 km east of Mayotte, resumed acquisition, it is a key station because the only one covering the crisis from east. With those eleven stations (Appendice 2), the network is still not optimal with gaps in azimuth and the lack of ocean bottom seismometers close to the events. Nevertheless, it allows sharper localization than those from global networks such as USGS, with a detection threshold lowered around the magnitude 3 instead of 4.5, and a catalogue complete from the magnitude 3.5.

From May 10 to November 14, we identified 1109 $m_l > 3.5$ events (Fig. 4). To those recorded at YMTZ we assigned a local magnitude $m_l = 0.9 \log(\text{pga}) + 2.56 \log(d) - 0.16$, with pga peak ground acceleration in m s^{-2} , and d, distance of the event, in km. This formula minimizes the scatters between m_l and the USGS m_b for the few tens of common events, occurring mostly in May and June. Our m_l is also aligned with the Seiscomp3 M_lh for the largest events by lowering the latter by 18%. There are 26 events also processed by the Global centroid moment tensor (G-CMT, Dziewonski *et al.* 1981; Ekström *et al.* 2012) with average scatter between m_l and M_w of 0.2 (Appendice 3).

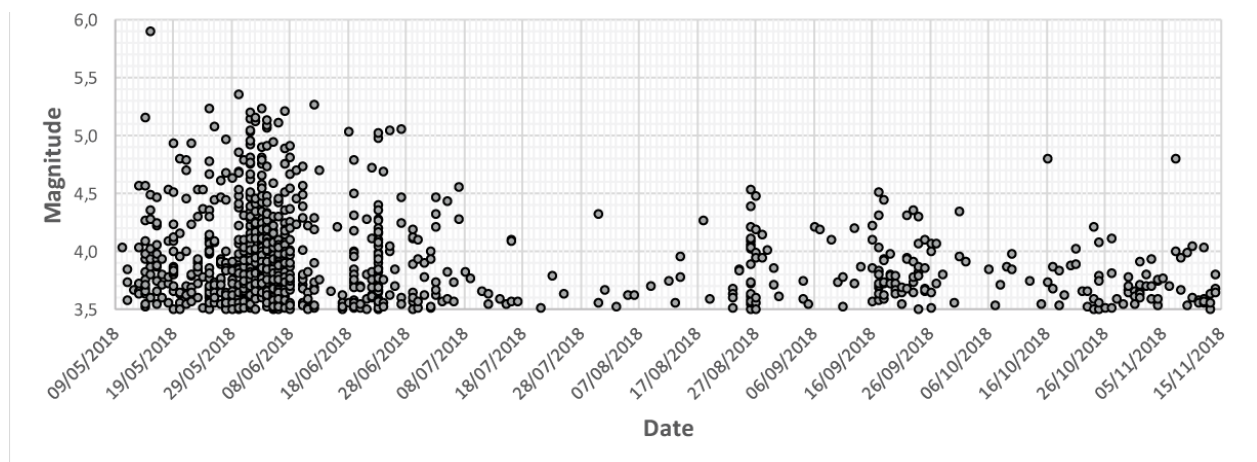


Figure 4. Magnitude of the 1109 $m_l > 3.5$ events recorded from 2018 May 10 to November 14.

The crisis started on 2018 May 10 morning with small events detected by YTMZ only. In the evening a $m_l = 4.3$ event not detected by the global networks, was the first event felt in Mayotte. From May 13 to 15 the activity increased gradually with four events with m_l between 4.5 and 5 (Fig. 4 and 5). The main event, and largest ever recorded in the Comoros, with magnitude $M_w = 5.9$ occurred on May 15. Then the seismicity was relatively steady during ~ 15 days with 10 to 30 $m_l > 3.5$ events per day. Two strong events occurred on May 20 and 21 ($M_w = 5.5$). Between June 1 and 7 the seismicity culminated with 50 to 80 $m_l > 3.5$ events daily. After June 7 the seismicity lowered. It increased again between June 19 and 27, with several $m_l > 5.0$ events. The period of July 10 to August 26 is quiescent with a sharp drop in the number and magnitude of the events. On August 26, eight events between $m_l = 4$ to 4.5 occurred, initiating a renewal of activity with two $m_l = 4.8$ events occurring on October 16 and November 7. However their contribution to the total moment release is low compared to the total.

For the seismic moment, we use the equation $M_o = 10^k$, with $k = 1.5 m_l + 9.1$ which gives the best fit to the available G-CMT values. The cumulated seismic moment for the whole period corresponds to an $M_w = 6.4$ event. The most active period, from June 1 to June 6, corresponds to an $M_w = 6.2$ event, more than the $M_w = 5.9$ of the largest event of May 15, whereas the maximum magnitude registered in this period is $m_l = 5.3$. In comparison, the cumulative seismic moment from 1977 to 2017 for the entire Comoros (between 42.5° E and 48° E) represents less than $M_w = 6.0$. The G-CMT fault planes are very similar for all events with, for the whole set, averages and mean scatters of $352 \pm 9^\circ$, $63 \pm 9^\circ$, $5 \pm 13^\circ$ for the plane 1 and $260 \pm 12^\circ$, $85 \pm 11^\circ$, $152 \pm 9^\circ$ for the plane 2 (Fig. 5). Both indicate strike slip on a steep fault. The corresponding tension axis is oriented $N34 \pm 15^\circ$, which corresponds to a most favoured faulting azimuth $N304^\circ$.

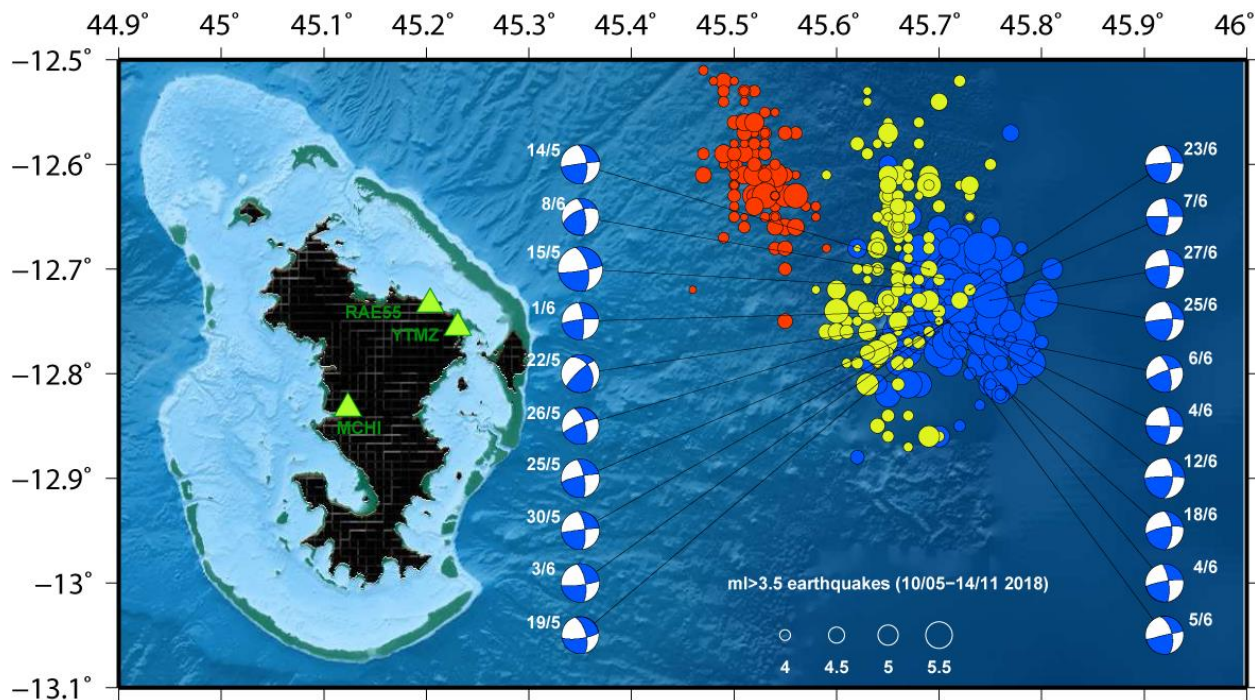


Figure 5. Map of the localized earthquakes of $m_l \geq 3.5$ from 2018 May 10 to November 14. The first cluster (blue) is active from May 10 to July 8, the second (yellow) from June 26 to October 30, the third (red) from July 5 to November 14. The G-CMT focal mechanisms correspond to $m_l > 5$ events, all occurring from May 14 to June 27. The bathymetry is from SHOM (2015).

Only 476 of the 1109 $m_1 > 3.5$ events were localized using crustal phases for distance ≤ 1200 km, 29 of them corresponding to $m_l \geq 5$ and 81 to $4.5 \geq m_l > 5$. The magnitude threshold for locating the events has been a function of the network evolution and the intensity of the seismic activity. From May 10 to May 30, all events with $m_1 \geq 4.5$ were localized, but not all those with m_1 between 4 and 4.5. During the intensive period of May 30 to June 7, we could not localize some events with m_1 between 4.5 and 5 because of the sparse network and too many repeating events leading to mixing seismic phases. From June 7 to June 27, all $m_l \geq 4$ were localized. After June 27 the catalogue of localized events is complete for all $m_1 \geq 3.5$ and the catalogue of magnitude is complete from $m_1 \sim 3.5$. We used the Seiscomp3 location algorithm LOCSAT (Nagy 1996) and the standard 1D velocity model IASP91 from Kennett (1991) as there is no velocity model available for the region. We fixed all events at 10 km depth, which allows the algorithm to converge. Our horizontal accuracy is 10-15 km with longitudes better constrained than latitudes because of the network geometry.

The seismicity is organized in three clusters (Fig. 5, Fig. 6). In the first one, active from May 10 to July 8, the events (blue dots) occurs in an area of ~ 20 km diameter, 45 to 65 km east of YTMZ. This cluster gathers all largest events of the crisis, and shows a gradual migration towards SE (Fig. 7), with a total of ~ 10 km shift for the period, while the G-CMT depths are evolving from 35 km to 15 km, which is beyond the error bars and a proof of upward migration. On June 26, the second cluster (yellow dots) starts west of the first one, closer to YTMZ (42- 55 km). The two clusters overlap in time until the first one ends on July 8. On July 5, a third cluster starts (red dots), with distance to YTMZ from 26 to 42 km, overlapping in time with cluster 2 until the latter ends on October 10. There is no evidence of epicentre migration in clusters 2 and 3, except at the beginning of 2 with some more westward events.

Fig. 6 shows that the cumulated seismic moment remains almost steady after July 8, and corresponds to an $M_w = 6.4$ earthquake. The more intense period of moment release is from June 1 to June 7 with an equivalent of $M_w = 6.2$. After a quiescent phase from July 13 to August 26, there is a resurgence of seismic activity at the end of August but with lower intensity and low contribution to the moment release (Fig. 4, Fig. 6). Because of network evolution until June 27, detection threshold have changed during the seismic sequence. This threshold is much higher for first sequence than for the following, whereas it has been the more intense seismic phase.

As a whole, the three clusters depict an activity migrating west-north-west during the onset of the crisis until early July. We made a b value analysis for the events of $m_l \geq 3.5$ by applying the Weichert (1980) method with magnitude steps of 0.1 (Fig. 8). The b value is 1.1 for the whole period and ~ 1 for cluster 1, typical values for tectonic seismicity. The b values for clusters 2 and 3 are 1.3 and 1.7 thus higher, and consistent with a volcanic context.

The 29 largest events ($m_1 \geq 5.0$) are listed in Appendice 3 with their G-CMT moment when it exists. All together they correspond to 57 % of the total moment release from May 10 to November 14. All occur during the first part of the seismic sequence, between May 14 and June 27. Most of them have similar strike slip focal mechanism indicating either right lateral shear along \sim EW structures or left lateral shear along \sim NS structures. The former is more consistent with the relative movements of the plates from either side of the archipelago, i.e. counter clockwise rotation of Lwandle plate with respect to Somalia plate (Saria *et al.* 2014), but the active structures that could be responsible for those mechanisms are not identified. There are other strike-slip focal mechanisms around Comoros since 1976 in the G-CMT catalogue (Fig. 3), the whole is consistent with a present-day \sim NE-SW regional extensional regime of the area.

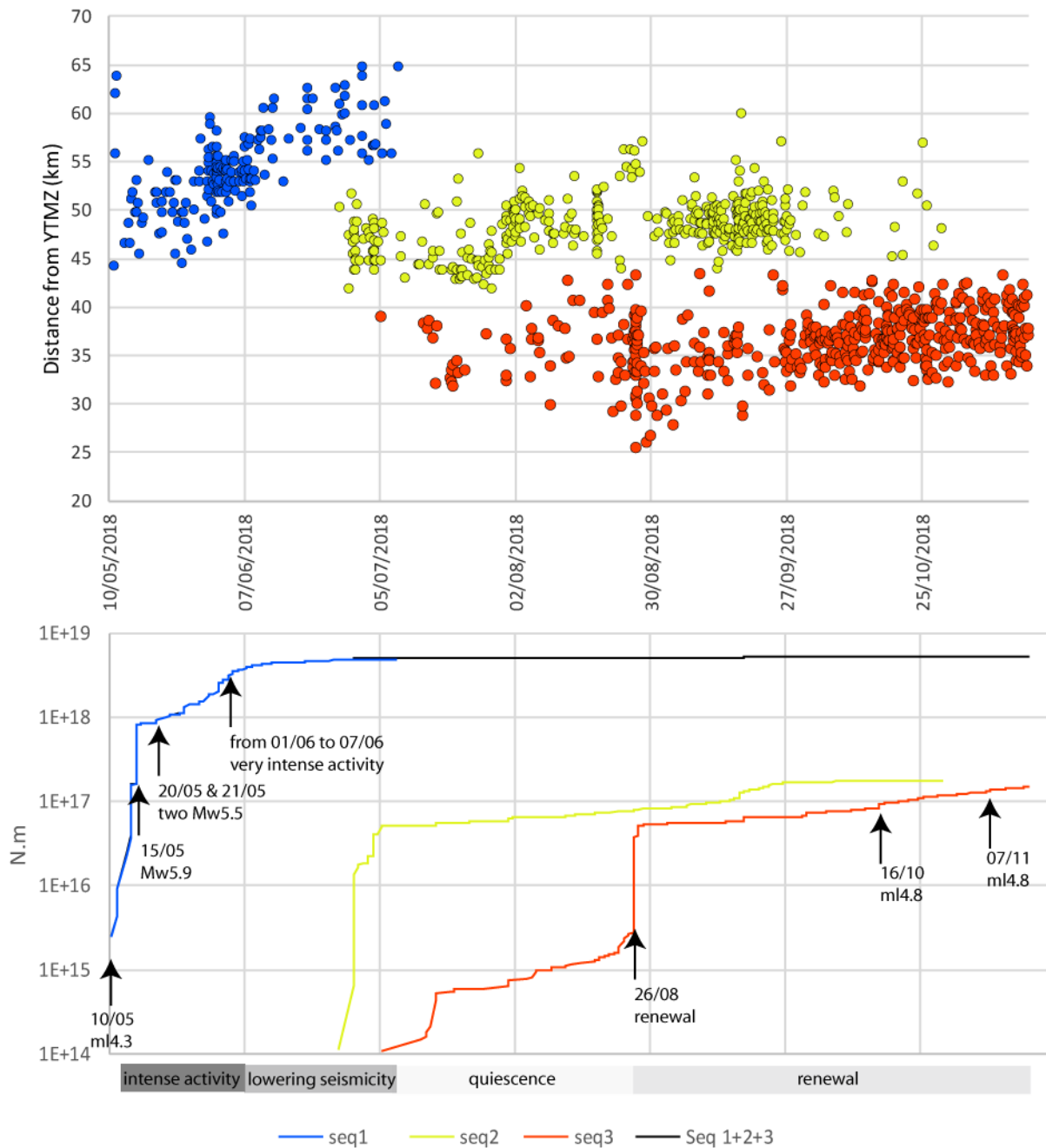


Figure 6. (top) Evolution of distance from YTMZ station with time. Three clusters are identified. Cluster 1 (blue) starts on May 10 and ends on July 8, with mean distance to YTMZ 55 km. Cluster 2 (yellow) starts on June 26 and ends on October 29 with mean distance to YTMZ 44 km. Cluster 3 (red) span from July to November 14 with mean distance to YTMZ 34 km. (bottom) Cumulated seismic moment for the three clusters and for the whole sequence (black).

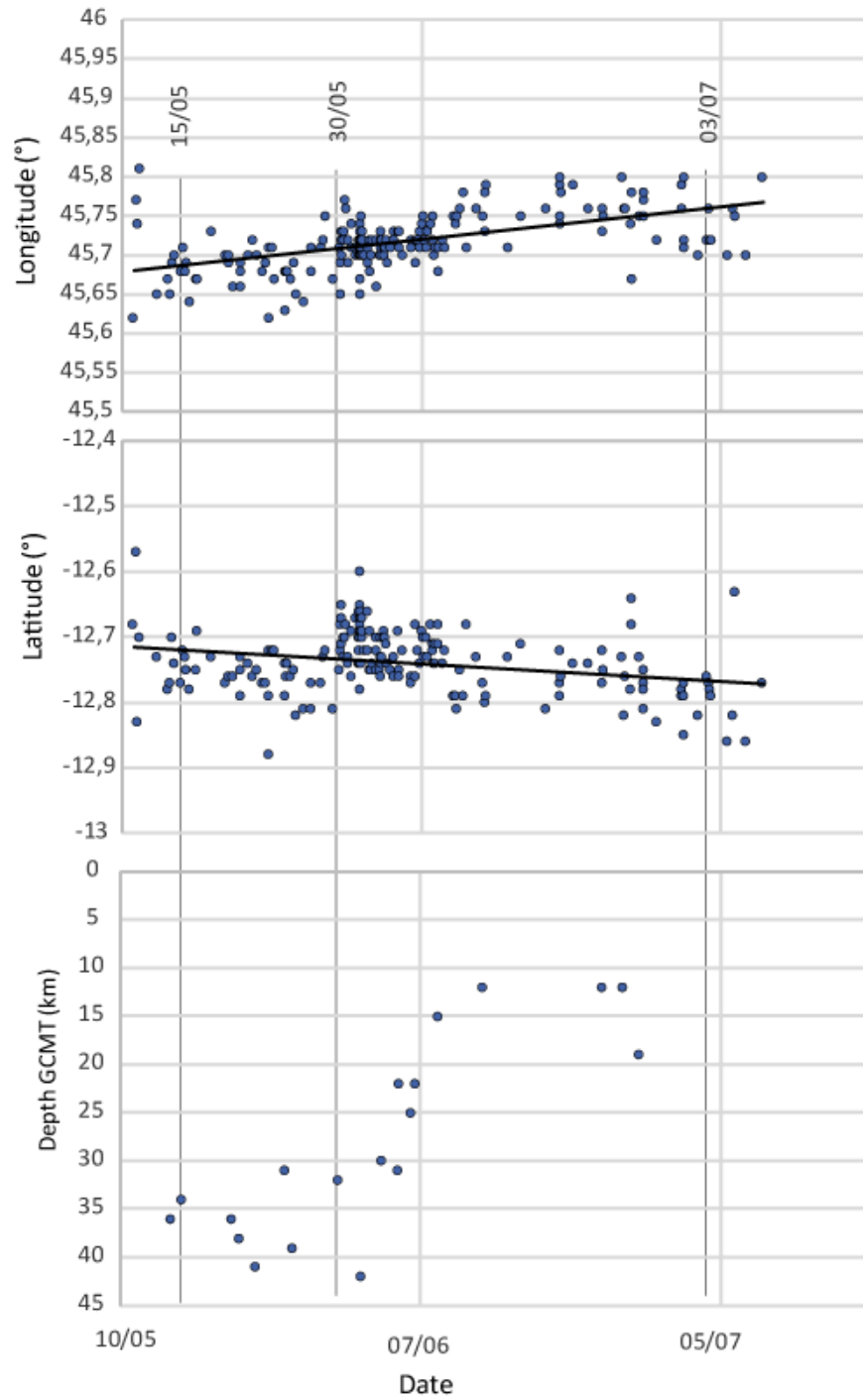


Figure 7. Eastward and southward migration of the seismicity within the cluster 1. Upward migration of the seismicity from early May as revealed by the depths determined by G-CMT for twenty events with $M_w \geq 4.9$ listed in Appendice 3.

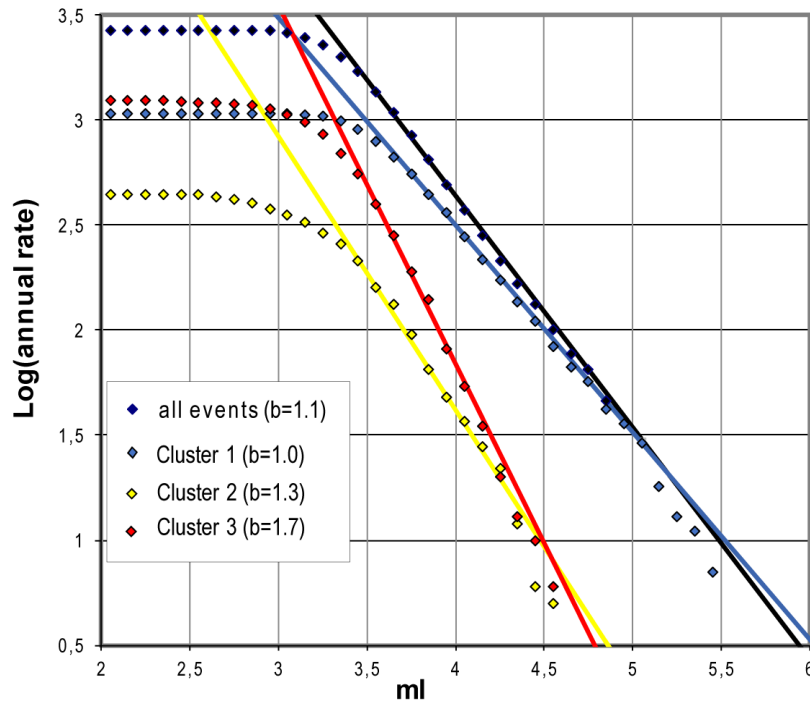


Figure 8. b values for the three clusters and the whole sequence

4. EPISODIC TREMORS

Several low frequency tremors (e.g. Tab. 1) have been recorded. The largest one, on November 11 (Fig. 9), recorded worldwide, awakened the interest of the seismological community and the media. None of those tremors is triggered by a strong earthquake, but there are earthquakes embedded in all tremors and all start with moderate and high frequency events. Those tremors might be dominated by long monochromatic very low frequency Rayleigh waves, event at short distance of the source.

Date	Start	End	Observations
02/09/2018	08:38	8:55	Several small high frequency events and different successive lobes of monochromatic low frequency waves. Peak at 0.062 Hz in the fast Fourier transform (FFT).
02/09/2018	11:12	>11:32	Many repeating high frequency events associated to a long sequence of monochromatic low frequency waves.
11/11/2018	09:27	09:47	Several small repeating high frequency events within the sequence of monochromatic low frequency waves. Peak at 0.062 Hz in the FFT. Waveform very similar to event 2.

Table 1. The three largest tremors recorded between May and November 2018. Timings are reported from local MCHI or YTMZ stations.

**November 11, 2018 event
East component**

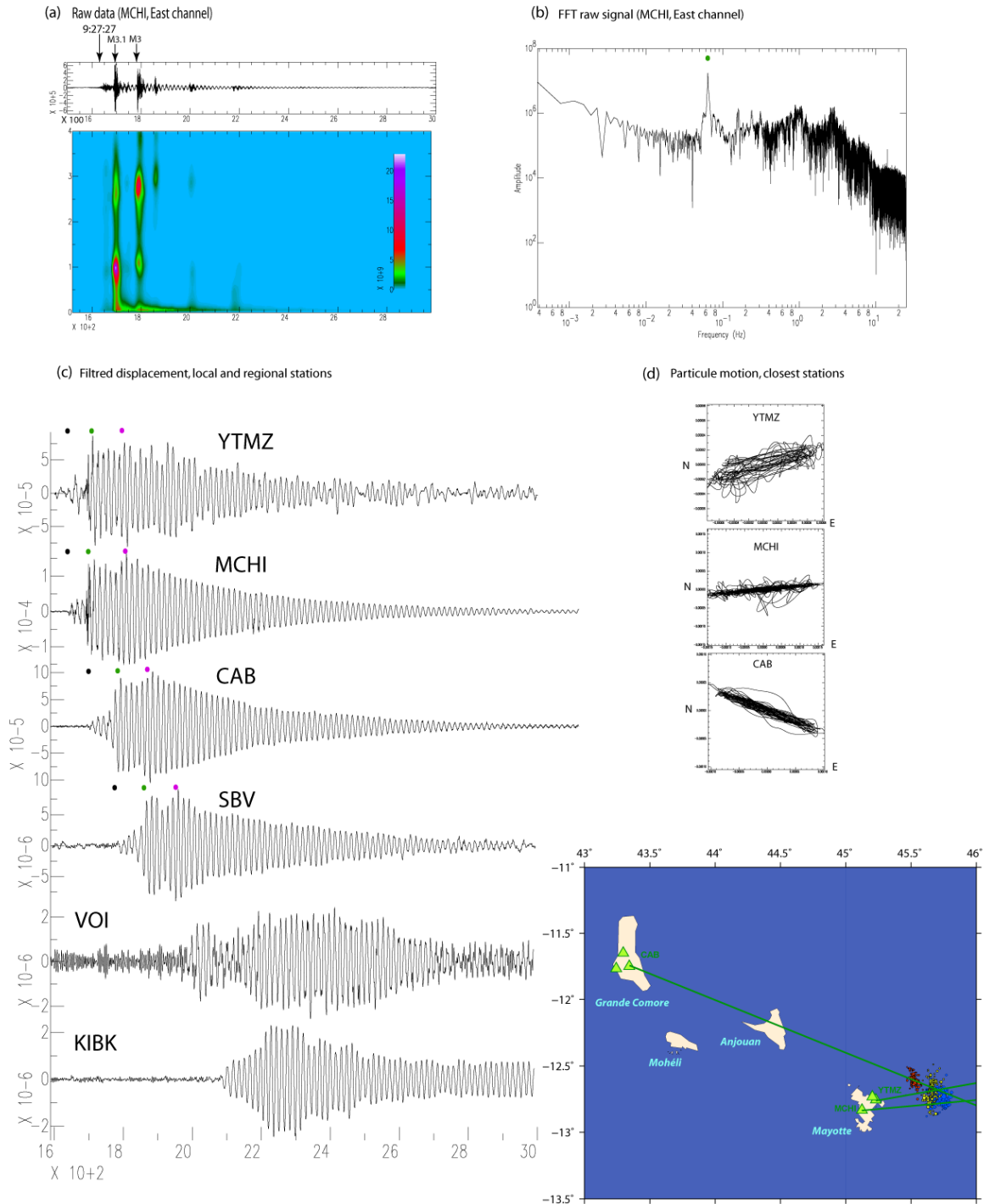


Figure 9. The 2018 November 11 tremor, (a) seismogram and spectrogram for the EW component of MCHI, (b) Fourier spectrum of the EW component of MCHI (peak at 0.062 Hz), (c) Displacements of local and regional stations, in meters. Black dots tag the initial excitation, green and purple dots its end and the beginning of the two embedded monochromatic damping phase, (d) Particles motions at YTMZ, MCHI and CAB and map showing the azimuth of the oscillation (green lines).

For the largest tremor of 2018 November 11, a small high frequency event occurs at 9:27:27 UTC, followed by small classical tectonic earthquakes, and then by the very low frequency monochromatic tremor that lasts around twenty minutes as shown by the EW record of MCHI (Fig. 9a). Two earthquakes of $m_1 = 3.1$ at 9:27:56 and $m_1 = 3$ at 9:29:30 stand out from the initial part of the tremor. They are located at 45.49°N , 12.61°S and 45.47°N , 12.58°S in the cluster 3. A third smaller event occurs at 9:30:50, followed by two very small ones that we could not localize, but well visible in Fig. 10. The spectrogram allows to separate the long low frequency signal of the tremor from the higher frequency shorter events. The Fourier spectrum (Fig. 9b) shows a peak at ~ 0.062 Hz, thus a period of ~ 16 s associated to the very low frequency tremor integrated to the signal (green dot).

Fig. 9c shows the EW component of seven local and regional stations. After integration, the signal was filtered in the band 0.05 to 1 Hz. In the case of YTMZ, which is an accelerometer, there was a first integration with filtering between 0.01 and 10 Hz. Three distinct phases can be distinguished in the records. An initial low frequency phase starts almost at the same time as the small high frequency signal that initiates the sequence (black dots especially that of MCHI). On local stations this initial phase lasts around 1 mn. The second phase is the one with the resonance and highest amplitude monochromatic waves (green dots). In the decay part of the signals, there are two embedded decays envelopes starting at the green and purple dots and lasting ~ 30 mn. The decay envelopes can be modelled (Fig. 10) with a model of damped oscillator following the equation $\exp(-t/\tau)$ with $\tau = 360$ s. From the physics point of view, this is compatible with the excitation followed by the free damping of a viscous fluid oscillating within a reservoir.

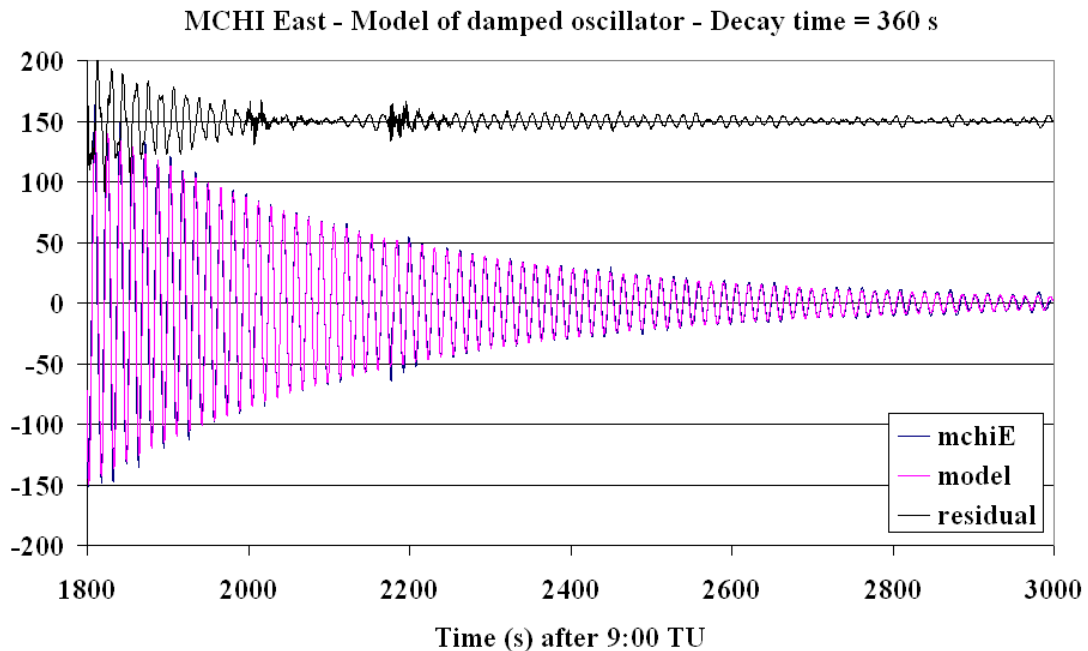


Figure 10. Modelling of the decay of the tremor for the east component of the MCHI station. A model of damped oscillator with decay time of 360 s fits well the data and permits to extract small earthquakes that occur during the course of the tremor.

Fig. 9d shows that, at the local stations, the tremor affects mainly the vertical and EW component, and much less the NS component, as shown by particles motion. The particles motion calculated for YTMZ, MCHI and CAB show how the oscillation is polarized during the monochromatic decay phase. The three green lines on the map are converging towards the location of the cluster 1, with the azimuth $N85^\circ$ from MCHI, $N80^\circ$ from YTMZ and $N112^\circ$ from CAB. The signal is noisier at YTMZ because it is an accelerometer and not a broadband station.

5. GROUND DEFORMATIONS

Six GNSS stations (Tab. 2) were operating in Mayotte at the beginning of the crisis, MAYG installed in 2014, all the others installed in early 2018. Their data are all gathered and routinely processed by the French IGN in the RGP (Réseau GNSS permanent, <http://rgp.ign.fr>).

Site	Name	Owner	Long	Lat
GAMO	M'Tangamouji	EXAGONE (TERIA)	45.0848	-12.7615
MTSA	M'Tangamouji	Precision Topo (Lél@sarl)	45.0789	-12.7616
KAWE	Kawéni	Precision Topo (Lél@sarl)	45.2251	-12.7670
MAYG	Dzaoudzi	CNES	45.2582	-12.7821
PORO	Poroani	Precision Topo (Lél@sarl)	45.1440	-12.8975
BDRL	Bandrélé	EXAGONE (TERIA)	45.1928	-12.9109

Table 2. The GNSS stations with name, owner and coordinates (location map in Fig. 12)

The time series in Fig. 11 were calculated in precise point positioning mode (PPP) with GIPSY 6.4. They present a strong common mode and four phases are visible, we call them A, B, C and D. Phase A spans from the origin of the GNSS observations (late 2013 for MAYG and early 2018 for all others) to the main earthquake of May 15. No precursory deformation is observed at any of the stations. During phase B, from May 15 to May 30, there is a small yet well visible (Fig. 12) deformation on the east component. During phase C, from May 30 to July 3, there is little horizontal deformation at the stations and a slight global subsidence. During phase D, starting on July 3, all stations show a large and steady drift mostly towards east and down.

Tab. 3 contains the velocity anomalies during phase D, obtained by linear fit. The time series of the NS component of the two southern stations PORO and BDRL indicate a significant velocity towards north during phase D unlike the other stations. As the EW velocities at all stations are very similar, we averaged them and at the first order we consider that the average vector represents the motion of the entire island of Mayotte at the barycentre of the six points located at 45.164°E and 12.813°S . Fig. 12 shows how the cumulated seismic moment correlates with the average east velocity of Mayotte.

Fig. 13 shows the evolution of the east versus north component, and east versus up. The figure is dominated by the large drift that occurs during phase D and shows clearly that this drift is linear during the investigated period. Vertical versus east component plots for phase B, C and D are aligned showing that the subsidence is not restricted to the phase D but occurs also, with lower intensity, during the phases B and C. In the north versus east, the situation is different and phase B, C and D occupy spaces not aligned together.

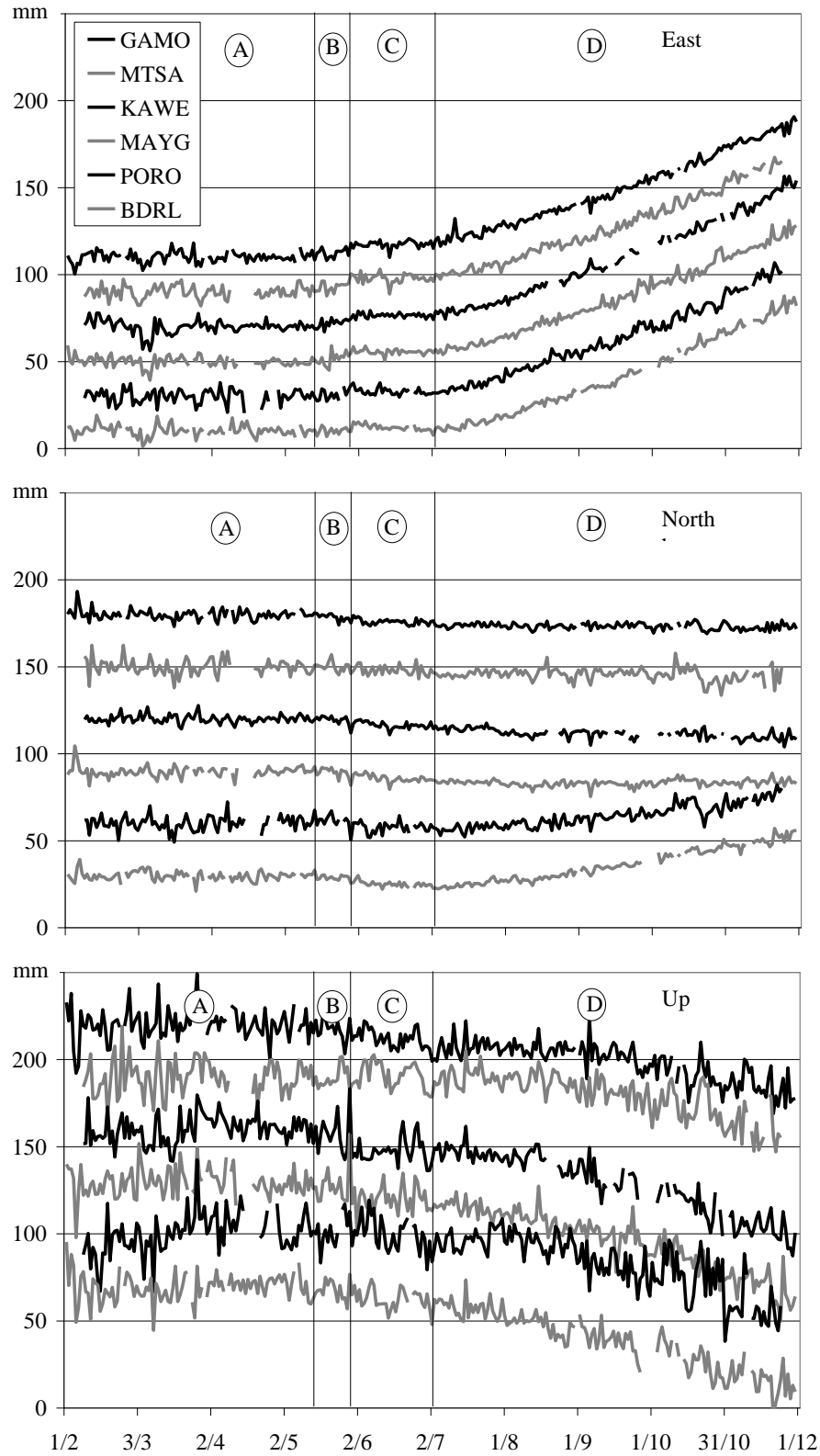


Figure 11. Time series of the coordinates of the six GNSS stations during phases A, B, C and D, corrected for the 2014-2018 velocity $v_E = 21.9 \text{ mm yr}^{-1}$ $v_N = 14.8 \text{ mm yr}^{-1}$ of MAYG.

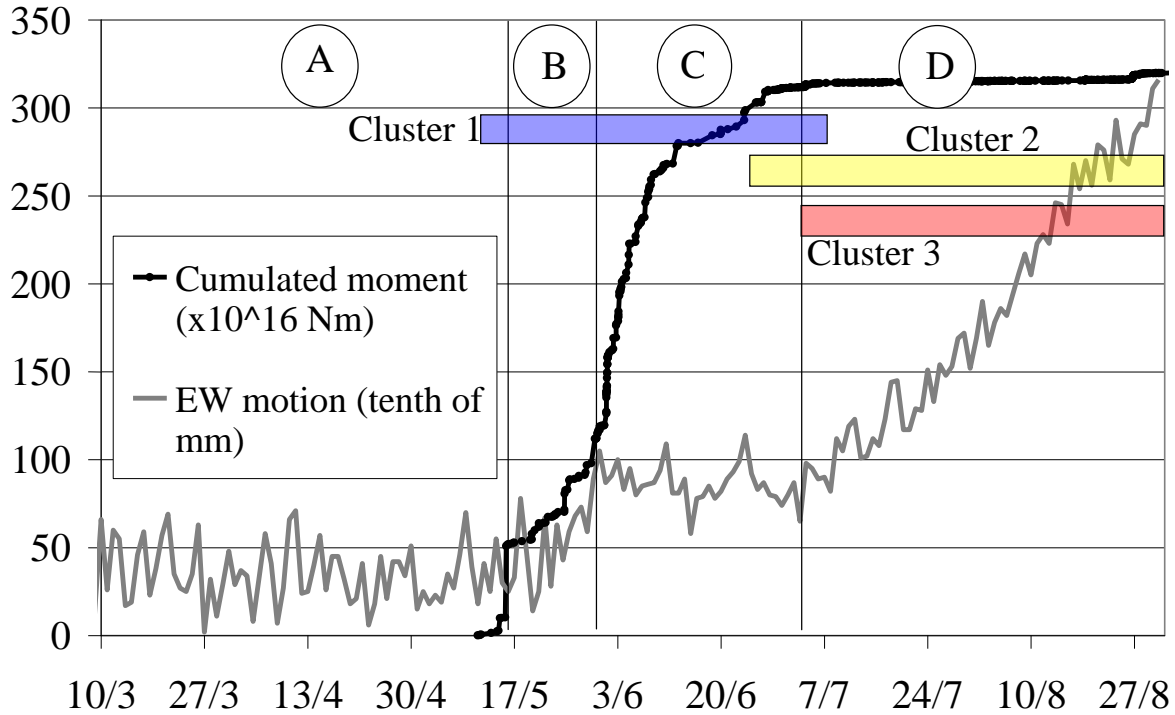


Figure 12. The phases of the crisis and the corresponding evolution of the cumulated seismic moment and average EW displacement of Mayotte. The scale of the left is for both the deformation (mm) and the seismic moment ($\times 10^{16}$).

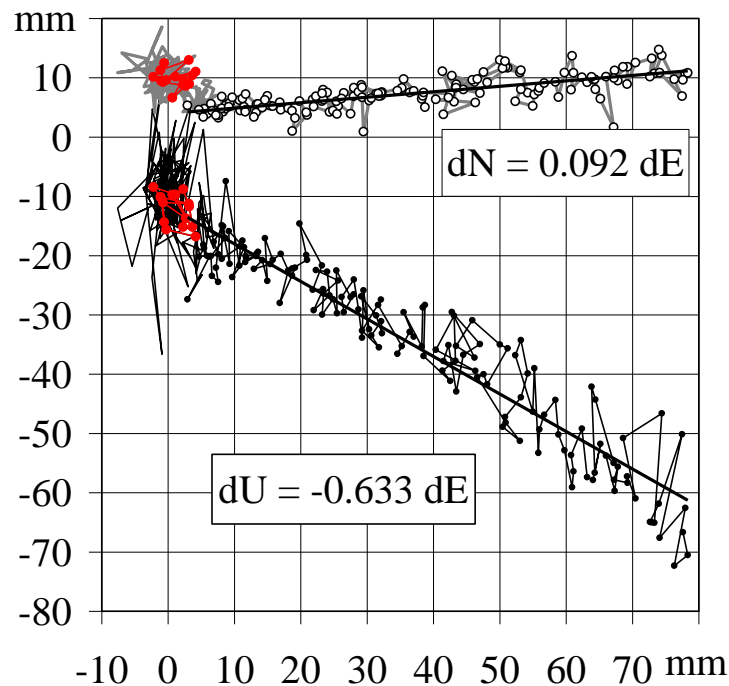


Figure 13. Ratio between horizontal and vertical motion during the phase D. For the vertical, this corresponds to a pitch of 33° between the barycentre of the six GNSS stations and the centre of the deflating source. The red dots correspond to the phase B.

6. MODELLING OF THE DEFORMATIONS

As we have seen in the previous sections, the seismicity and ground deformations are organized in four main phases. We associate them to the processes of fracturing (phase B), magma ascend (phase C) and eruption (phase D). In the following we model the ground deformations associated with the phases B, C and D.

We first model phase D as it is the one that dominates the ground deformation. We use the simple and widely used Mogi (1958) model that assumes a deflating point source buried in an elastic half space. Our data constrain well the source azimuth, pitch and deflation but not its distance to the stations. This is because all GNSS stations are in the same azimuth. In consequence there is a family of solutions that fits almost equally well the data from longitude 45.55° to longitude 45.75° , with the source depth varying linearly from 25 to 40 km when browsing this range of solutions. If now we blend in our inversion 50% of cost of fit of the Mogi model with 50% of cost based on the crossing place of the horizontal vectors (Fig. 14), using as metrics the minimization of the cross product of the displacement vectors and the vectors source-station, we find a best fitting source at 45.590° E, 12.777° S and 28 km depth. The corresponding emission rate is $82 \text{ m}^3 \text{ s}^{-1}$. The blending of the two criteria in the inversion is interesting because the unconstrained Mogi modelling tends to pull the model further east (to give a better fit at one single observation which is the EW motion of MAYG, which means that this data has to be highly trusty), while the crossing of the horizontal vectors pulls the solution the other way. The combination of both gives a stable solution with mean residuals of 25, 5 and 20 mm yr^{-1} in the east, north and up components respectively (Tab. 3).

Site	Phase D velocity (mm/yr)			Phase D model (mm/yr)			Residuals (mm/yr)		
	East	North	Up	East	North	Up	East	North	Up
GAMO	172	-4	-69	153	-5	-78	19	1	9
MTSA	173	-5	-83	151	-5	-76	22	0	7
KAWE	202	-12	-139	227	-6	-160	25	6	21
MAYG	176	2	-133	248	4	-192	72	2	59
PORO	180	51	-114	166	46	-96	14	5	18
BDRL	184	77	-125	184	63	-119	0	14	6

Table 3. Velocity anomalies at the GNSS stations of Mayotte during the deformation phase D from 2018 July 3 to November 14 assuming a linear trend (observations, model and residuals).

For phase C (May 30 to July 3), we interpret the deformation (Tab. 4 left) as due to the ascent of magma in a conduit connecting the deep reservoir to the sub-surface, combined with the deflation of the reservoir of a similar volume. This scenario is supported by the fact that, in that period, the EW motion is nearly zero while there is a slight vertical motion (Fig. 11) of 7 ± 4 mm. Such ground motion can be explained with a magma body migrating upward without emission at the surface, thus without global change of volume. As the above mentioned subsidence rate is 55% of that of phase D and mostly attributable to the deflation of the reservoir (because a shallow source cannot produce vertical changes at GNSS stations, especially at that distance), we assume that the horizontal rate associated to the deflation is also 55% of that of phase D. This allows us to evaluate what we call the C_reservoir contribution in Tab. 4 (right). By difference, the remaining part is what we call C_conduit. We interpret it as the elastic response measured at the

GNSS stations to the opening of the feeding magma conduit (Fig. 14) from the top of the chamber to the sub-surface and the further opening of the shallow dykes and possibly sills. As the emission rate is of $82 \text{ m}^3 \text{ s}^{-1}$ in phase D, rescaled by 55% it is $45 \text{ m}^3 \text{ s}^{-1}$ during phase C, which means that the volume injected in the channel and shallow dykes and sills, is $0.16 \cdot 10^9 \text{ m}^3$ during the 42 days of phases B and C.

We model the C_conduit deformation by using the Okada (1992) formalism and the inversion code developed by Briole *et al.* (1986, 2017). As our GNSS stations are far from the source, we do not have a good resolution for the shape of the conduit. We assume that it is an elongated dyke buried at a depth of 22 km depth (at the top of a deflating chamber that we assume of 12 km diameter) with its tip 2 km beneath the seafloor. As a priori azimuth for the conduit we use $N304^\circ$ which is perpendicular to the tension axis, and the best fitting azimuth found by our inversion is $N318^\circ$, yet loosely constrained because of the distance of the GNSS stations. The best fitting solution for the width of the conduit is $4 \pm 2 \text{ km}$ and its opening $1.62 \pm 0.7 \text{ m}$. Thus the best fitting volume of the modelled conduit is $0.13 \cdot 10^9 \text{ m}^3$, 20% less than the a priori value. The root mean square (r.m.s.) scatter of the residuals is 3 mm for the horizontal components and 6 mm for the vertical. In the uppermost part of the crust we suppose that the conduit extends laterally in an shallow dyke $\sim 20 \text{ km}$ long, connecting the cluster 1 to the cluster 3 (the one still active at the time of this paper) along the same axis $\sim N318^\circ$. This dyke could accommodate the missing $0.03 \cdot 10^9 \text{ m}^3$. The short lived cluster 2 might correspond to another dyke or to a sill.

There is no means with our geodetic data to resolve precisely the characteristics of the shallow channels (dyke and or sill), because their volume is small for the distance and because they do not affect the vertical component. From the vertical GNSS data, we can only assess that there cannot be large horizontal injection at depth (e.g. 10 km long at 10 km depth) because this would give a geodetic signature that is not observe.

Site	Observed Total phase C			C_reservoir (*)			C_conduit (observation)			C_conduit (model)			Residuals		
	East	North	Up	East	North	Up	East	North	Up	East	North	Up	East	North	Up
	mm	mm	mm	mm	mm	mm	mm	mm	mm	mm	mm	mm	-3	-2	-6
GAMO	0	-4	-9	11	0	-4	-11	-4	-5	-8	-2	1	-2	-2	9
MTSA	1	-4	5	11	0	-5	-10	-4	10	-8	-2	1	0	1	-2
KAWE	0	-3	-8	13	-1	-9	-13	-2	1	-13	-3	3	6	-2	-5
MAYG	0	-6	-9	11	0	-8	-11	-6	-1	-17	-4	4	2	1	5
PORO	0	-2	0	11	3	-7	-11	-5	7	-13	-6	2	-2	-7	-4
BDRL	-6	-7	-10	12	5	-8	-18	-15	-2	-16	-8	2	East	North	Up

Table 4. Deformation in phase C split in two contributions: deflation of the reservoir & inflation of the feeding conduit. The values in the column C_reservoir (*) are estimated by scaling by 55% over 42 days the rates of the phase D (from Tab. 3). The modelling of the conduit parameters is assuming that the centre of the conduit is above the centre of the reservoir.

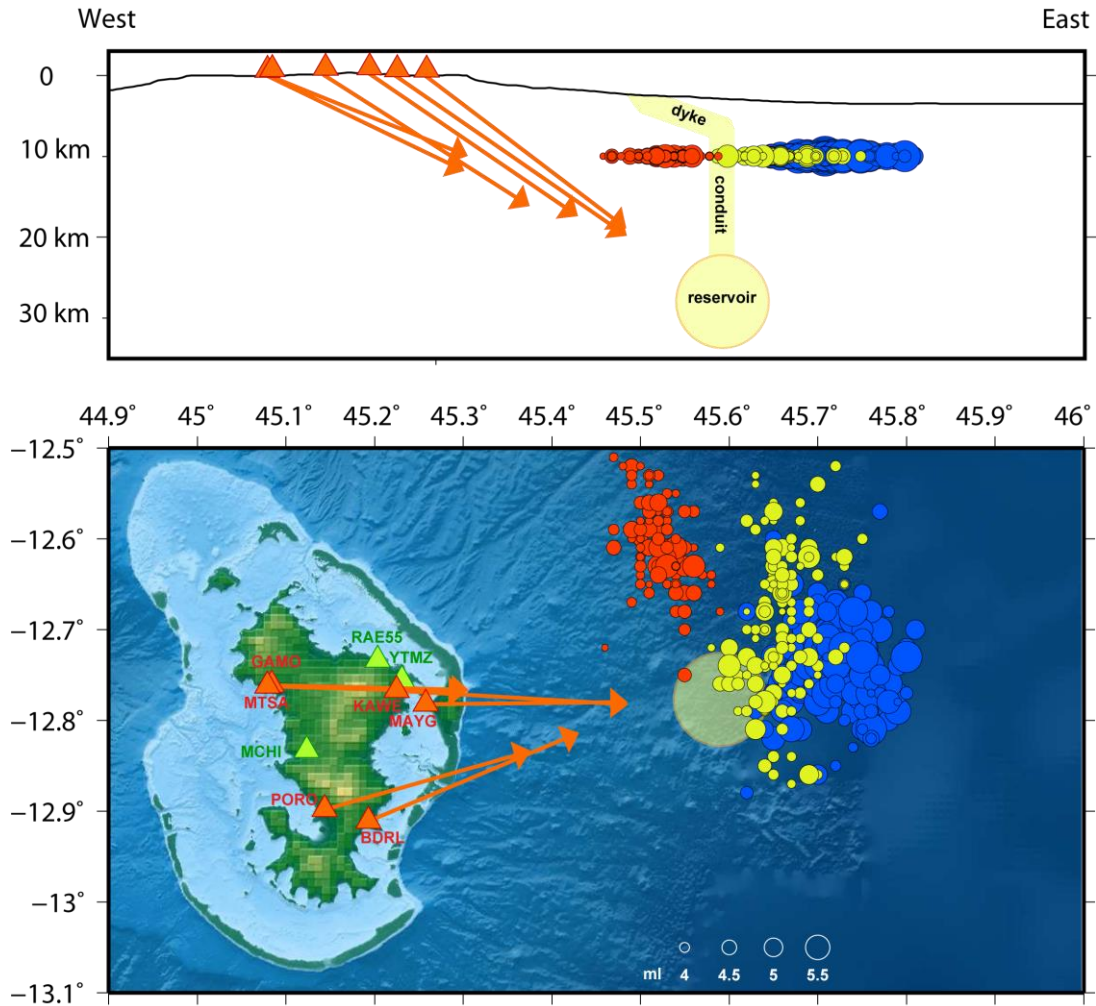


Figure 14. Orange vectors are proportional to the vertical (top) and horizontal (bottom) velocity anomalies during phase D from 2018 July 3 to November 14. The clusters 1, 2 and 3 with $m_l > 3.5$ events between May 10 and November 14, 2018 are plotted in blue, yellow and red. Their depth (top) is fixed at 10 km because unresolved by the monitoring network. The bathymetry is from the Homonim project (SHOM, 2015) completed by Gebco_2014 data. Green triangles indicate the seismic stations, orange triangles the GNSS ones. Yellow circle correspond to location of the magmatic chamber (assuming a radius of 6 km) as inferred from the GNSS velocities during phase D. Yellow surfaces (top) represent the conduit connecting the deep reservoir to the sub-surface and a laterally extended shallow dyke connecting clusters 1 and 3.

For phase B during which a small yet clear deformation is observed, mostly from May 25 to May 30, we used an Okada (1992) model with the following parameters: same location and geometry as phase C, thus rectangular fault elongated vertically of 20 km length and 4 km width. The best fitting slip is 0.85 m of pure strike-slip. Assuming a rigidity of $3.3 \cdot 10^{10}$ Pa, the corresponding moment is $M = 224 \cdot 10^{16}$ Nm a value twice as large as the total seismic moment cumulated on May 30 but compatible with the cumulated moment few days later on June 2. When relaxing the azimuth from its initial value of $N318^\circ$ (inherited from phase C modelling), the best fit is obtained with $N341^\circ$, which corresponds to an azimuth of the tension axis oriented $N26^\circ$, slightly

smaller than those found before, but consistent, and very consistent with the G-CMT focal mechanisms. With both geodesy and seismology, we have no means to discriminate between the conjugate planes, and the upward fracturing during phase B might well involve cracks on a blend of the two families of planes.

Site	Phase B			Model			Residuals		
	East	North	Up	East	North	Up	East	North	Up
	mm	mm	mm	mm	mm	mm	mm	mm	Mm
GAMO	5	-2	0	3	-1	0	2	-1	0
MTSA	5	0	0	3	-1	0	2	1	0
KAWE	6	-3	0	6	-1	0	0	-2	0
MAYG	3	-1	-1	6	-2	0	-3	1	-1
PORO	2	-2	0	1	-1	0	1	-1	0
BDRL	4	-1	0	1	-1	0	3	0	0

Table 5. Deformation during phase B from May 15 to May 30. We assume that the fault has the same geometry as the conduct of phase C, thus a rectangular fault of 20 km height and 4 km extension, and slip 0.85 m.

7. DISCUSSION

The evolution in time and space of the ground deformation observed in Mayotte, 45 km east of the crisis, allows to distinguish four phases in the phenomenon and to link them to the three observed seismic clusters. Because of the poor coverage in azimuth, the longitude of the deflation source is not easy to assess. However, as our two criteria (best fitting Mogi source and horizontal crossing of the vectors) are leading in opposite directions, we believe that our localisation of the deflating source is resolved within a few kilometres in a robust way. Subsequently, its depth is constrained accurately by the pitch of the deformation and the trade off between distance and depth in the model (Fig. 13). Its azimuth is well constrained by the azimuths of the GNSS vectors.

Our modelling assumes that the source is a point, which is of course not the case, but we cannot resolve this with GNSS as, at such distance, a source of several kilometres of radius is indistinguishable from a point source. We assumed that the source diameter is 12 km, because this is typical value used in literature for deep reservoirs, based in particular on the size of many calderas that can be seen on Earth e.g. the Phlegraean Fields caldera in Italy. A significant lateral extension of the reservoir is also needed to explain the tremors if we assume that they are originated in the chamber.

With a source at 28 km depth and 6 km radius, the magma extracted from the top of the reservoir would be coming from a depth of ~22 km. As our model is made assuming a half space and neglects the real topography, this ~22 km should be regarded as the depth beneath the seafloor at that location, thus ~25 km beneath the sea surface as the water thickness is around 3 km above the inferred reservoir.

The phase D, which runs since almost eight months at the time of this paper, is the one with the lowest cumulated seismic moment. This indicates that the fracturing from the reservoir depth to

the subsurface is terminated and the moderate remaining seismicity mostly concerns the eruption zones at shallow depth.

With 6500 m^2 for the best fitting section of the feeding channel and $82 \text{ m}^3 \text{ s}^{-1}$ for the emission rate, the speed of magma ascend is 0.013 m s^{-1} for the phase D since July 3 and half between May 30 and July 3. Such low speed of magma ascent has been observed elsewhere and is discussed by Gonnermann & Manga (2013), in particular from the analysis of the crystals in the erupted magmas. As the emission rate of phase D is twice that of phase C, the products of phase D might exhibit less advanced crystallization with respect to those of the phase C. Future analysis of the lava flow, if some lava reached the seafloor and samples can be collected, might tell more about this speed and provide confirmation of our estimate.

The GNSS data provide constraints on the timing of the creation of the channel that opened the way to the magma from the reservoir to the surface. This occurs during phases B and C, thus between May 15 and July 3. Moreover the change in the signature of the deformation suggests that the filling of the conduit start at the end of the phase B, during the peak of seismicity (and rock fracturing) that occurs between May 30 and June 7. The fracturing of phase B can be explained geodetically without the need of filling the ruptured faults.

The steadiness of the deformation in June implies a steady rate (within our observational uncertainties) of the magma release from the reservoir during that month. This suggests that the cracks moved towards the surface and started being filled according to a relatively smooth process. The rate of magma release is less in June, approximately half, than the one estimated after July 3. In other words, the flux in the feeding channel has doubled in July once the path to the surface opened, and the eruption started. The timing of the start of the eruption comes from the beginning of the large ground deformations, thus when there is not anymore a balance between the volumes collected at large depth in the reservoir and those stored at shallow depth.

We have no strong constraints on the geometry of the feeding conduit. Even a cylinder would fit reasonably well the observations. However the best fitting model is an elongated vertical conduit, starting arbitrarily at the depth of 22 km on top of the reservoir, and ending at a depth 2 km, the latter value being estimated by the inversion, yet loosely. What is well constrained instead by the inversion, and little dependent on the shape of the source, is the volume of the conduit, $0.13 \pm 0.01 \cdot 10^9 \text{ m}^3$, and therefore also its section, 6500 m^2 . Assuming a pipe shape, its diameter would be 90 m. It is difficult to figure out how such cylinder could develop in a few days within along two tens of kilometres in a crust not having been perforated by magma in the recent geological times. Therefore it is much more likely that the feeding conduit is a dyke and this is the reason why we made this assumption. The best fit for this dyke is a horizontal width of 4 km, an opening of 1.62 m, and an azimuth of $N318^\circ$. The azimuth is loosely constrained, because the conduit is narrow, but consistent with the overall SW-NE extension inferred from the focal mechanisms and the orientation of the extension from GNSS and the tectonic structures. The cluster 2 could be related with the injection at shallow depth of dyke unfruitful of a sill before the eruption eventually starts at the time and location of the cluster 3.

A better instrumental coverage and offshore observations will permit to better constrain local and regional seismicity and to characterize active volcanic and tectonic features, their link and potential induced effects (volcano flank instability, caldera formation, tsunami, induced earthquakes on active tectonic features). For GNSS, adding stations at Grande Comore, Anjouan and especially Glorieuse islands, will improve the capability to locate the deflating source. The

predicted deformation rates (Tab. 6) are compatible with a capability of anomaly detection if that anomaly lasts six or more months, which might still justify the deployment of instruments even if eight months of eruption have passed already. It will be important to maintain those instruments active for one year or more after the end of the crisis in order to distinguish the transient rate from the long term rate.

Site	Long	Lat	Distance (km)	vE (mm yr ⁻¹)	vN (mm yr ⁻¹)
Grande Ile Glorieuse	47.30	-11.58	215	-15	-12
Mutsamudu (Anjouan)	44.39	-12.17	160	29	-14
Moroni (Grande Comore)	43.25	-11.71	260	9	-4

Table 6. Predicted horizontal velocities anomalies predicted at three nearby islands, assuming the deflation rate of $82 \text{ m}^3 \text{ s}^{-1}$ of phase D.

The seismicity of the cluster 1 is shifted by 14 km towards east and 4 km towards north with respect to the location of the reservoir, while one would expect to see them superimposed. This shift is large but within the error bars of the localisation of the events, given the weakness of the network and also the standard velocity model that has been used while not necessarily adequate for that situation. In the Fig. 15 we moved by two thirds of the above shift, i.e. 10 km and 3 km towards west and south respectively, the centres of the clusters 1, 2 and 3, assuming that this might represent the best compromise between the constraints from the geodetic modelling and the uncertainties in the localisation of the seismicity. In this case, the centre of the cluster 3, the one still active after eight months, and likely to correspond to the area of the eruption, would be located at 45.44°E , 12.64°S at ~ 22 km of the northern cape of Petite Terre, in an azimuth $\sim \text{N}45^\circ$. This location is in the slope of the volcano of Mayotte, with a seafloor at ~ 2000 m depth, in an area where small seamounts of a few hundred metres exist in the bathymetry (Audru *et al.* 2006). Those existing seamounts might correspond to previous eruptions sharing some similarities with the current one.

The G-CMT focal mechanisms are associated to the largest events of May and June. Those events belonging to the cluster 1 during which there is a 10 km south eastward migration of epicentres (Fig. 7). This migration could potentially be an artefact due to the assumption of uniform 10 km depth for all events. The localizations, performed with a sparse network, do not allow to distinguish between migration upward or towards the southeast. However there are evidences of upward migration: first the depths of the events determined by G-CMT, all occurring during the cluster 1, show a clear upward migration (Fig. 7), especially from early to end of June; second, the coda at VOI become longer as a function of the date, which could be interpreted as an effect of the sensitivity of the surface waves to the source depth.

The centre of cluster 3 is at ~ 20 km of the centre of cluster 1 in the azimuth $\text{N}305^\circ$. The shallow dyke active since July might therefore have comparable length and azimuth. However this cannot be assessed geodetically because the volume involved is too small, especially in comparison to the volume involved in the deflation, and because it is shallow. The dyke could be located at shallow depth at the top of the crust, just below the 1 to 2 km of sediments that exist at the seafloor in the area. Assuming a length of 20 km, a height of 1.5 km and a width 1m, it would represent a volume of $0.03 \cdot 10^9 \text{ m}^3$, which, added to the $0.013 \cdot 10^9 \text{ m}^3$ of the vertical feeding

channel, would balance the $0.016 \cdot 10^9 \text{ m}^3$ released by the reservoir during the phase C. Nearly all focal mechanisms made by G-CMT indicate an extension axis oriented $\sim N50^\circ$. The perpendicular azimuth, $N310^\circ$, is therefore the most favourable axis for the feeding dyke, thus very close to the abovementioned $N305^\circ$. This azimuth is consistent with some topographic features observed in the bathymetry east of Mayotte, e.g. the Jumelles seamounts, and with that of dykes exposed onshore north of Mayotte (Nelhig *et al.* 2013). It is also consistent with the overall axis of the Comoros and volcanoes and roughly perpendicular to the relative motion measured by GNSS (Fig. 2) in the azimuth $N50^\circ$ across the Comoros. Malod *et al.* (1991) mapped $N10^\circ$ structures and interpreted them as transform faults inherited from ancient oceanic spreading in the Somalian basin. This azimuth fits with the G-CMT of the large events of phases B and C. Therefore it is possible that some ancient structures were reactivated and opened to give way to the rising magma.

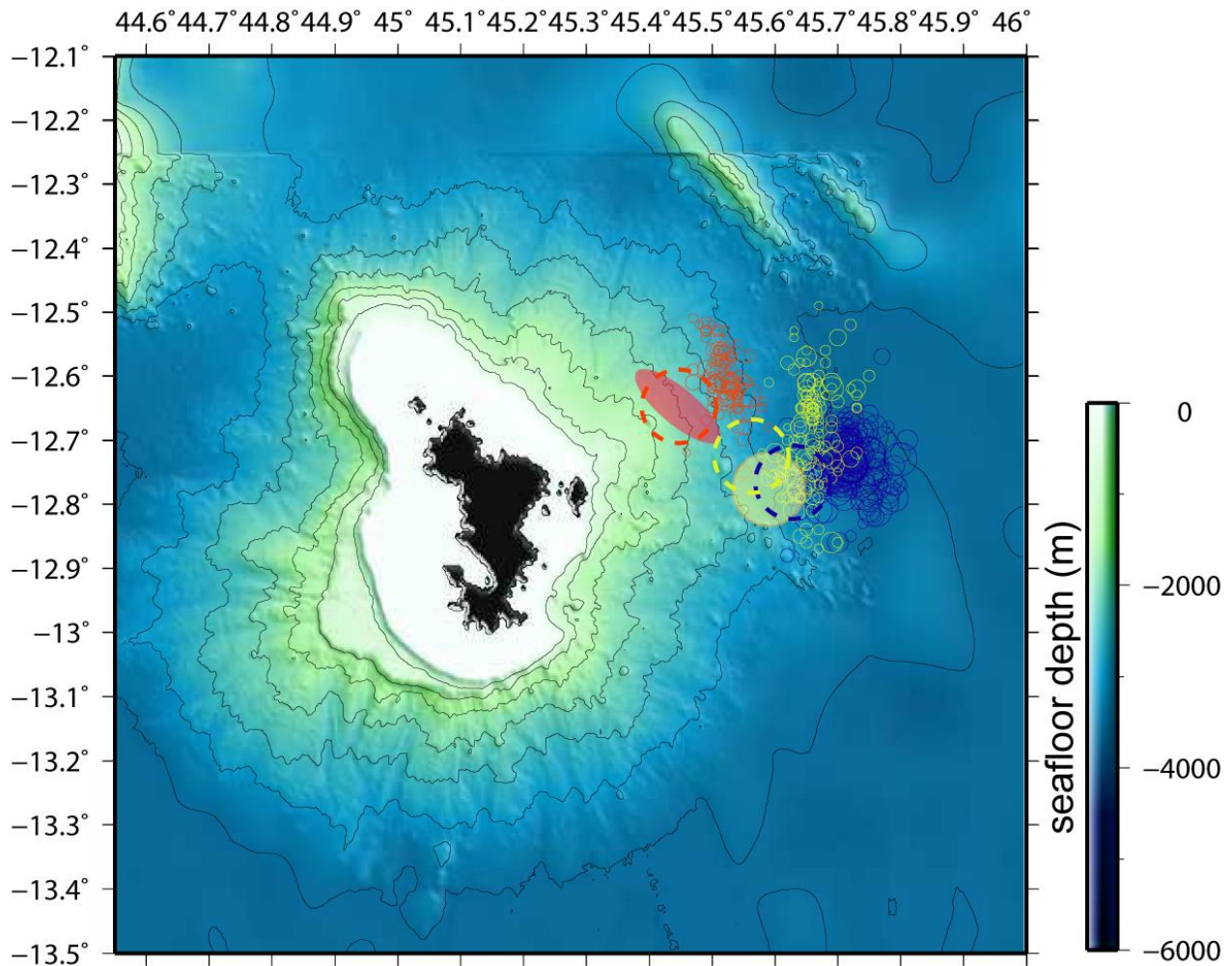


Figure 15. Yellow full filled circle represent the centre of deflation inferred by the GNSS data. Small open circles represent seismicity ($m_l > 3.5$) and large opened dashed areas represent hypothetical position of the centers of the three clusters shifted by 10 km westward and 3 km southward with respect to their native location, so as to bring closer geodesy and seismology, within their respective uncertainties. The eruption might take place within the red ellipse, connected to the vertical conduit by a ~ 20 km long dyke. The bathymetry is from SHOM (Homonim project) and Gebco_2014.

With a rate of 45 m³ s⁻¹ during 42 days and then 82 m³ s⁻¹ from July 3 to November 14, at the latter date the total volume extracted from the chamber was 1.15 km³.

There is no precursory deformation before the crisis visible in the time series of MAYG (which starts in late 2013) or the other stations (which all start in early 2018)

The constraints on the geometry of the deep feeding channel, and the possible shallow dyke, can be used as a priori geometric model for the interpretation and modelling of the tremors. Those could be generated by an oscillation in a long horizontal shallow dyke or in the reservoir, hardly in the vertical conduit as the particles motion does not support well the hypothesis of vertical vibrating source. We have seen that, based on the GNSS data, the existence of tremors, the high *b* values, the deforming phase D, corresponding roughly to the clusters 2 and 3, can be explained by the deformation of a deep magma chamber. Various hypotheses can be proposed in order to explain the source mechanism of such a signal, including resonances and transports of volcanic fluids in magmatic systems (slow collapse of the roof of a magma chamber along ring faults, resonance of magma chamber induced by small earthquakes or dyke injections, e.g. Shuler *et al.*, 2013). Moreover, on 2018 November 11, low frequency monochromatic waves of period ~16 s, recorded worldwide by broad-band stations, were emitted from the same area, potentially due to resonance in a magmatic chamber of appropriate size.

8. CONCLUSIONS

We believe that the 2018 crisis is associated to an eruption, despite the fact that we do not have direct observations so far. It might be the offshore eruption with the largest volume ever documented.

Unusual seismic sequences are reported in literature in different contexts, e.g. along oceanic transform faults (Roland & McGuire 2009) or in volcanic areas such as Bardarbunga, Iceland (Gudmundsson *et al.* 2014), Hakone volcano, Japan (Yukutake *et al.* 2011), Afar, Ethiopia (Ayele *et al.* 2007. Ahmed 2016). Seismic swarms are commonly associated to fluids intrusion, including magma (e.g. Hainzl 2004; Toda *et al.* 2002). The 2018 crisis of Mayotte shows some similarities with past telluric crisis having involved dyke intrusions. For example, during the 2005-2010 telluric crisis in Afar (Grandin *et al.* 2011; Ahmed *et al.* 2016) there were six different phases of dyke injection and magma ascend, as in our case the cluster 1 and 2 may correspond to two different phases of shallow injections. In the case of the eruption of 2000 at Izu, Japan, Toda *et al.* (2002) showed that the dyke propagation was associated with both normal and strike-slip earthquakes. This crisis shows also similarities with that of 2011-2015 at El Hierro, Canary island where the activity also started below 20 km depth and was also characterised by several phases of intrusion and eruption (Klügel *et al.* 2015). The 2018 crisis of Mayotte is also showing the dominance of strike slip events during all the fracturing period of phases B and C. Such dyke related seismicity is also sometimes producing the so called “dogbone seismicity distribution” where normal faulting events around the dyke (normal faults parallel to dyke) coexisting with strike slip events around it.

If the eruption lasts one year, which is typical for volcanic eruption, the subsidence of Mayotte will exceed 0.1 m which is large but not critical for the inhabitants and infrastructures, and the

total volume emitted will exceed 2 km^3 . Such volcanic event near a coast is the largest ever observed and it may be a major teacher for the understanding of how off-shore volcanoes work.

Although the inferred deflation source is deep, not having the experience of previous similar events, we believe that we cannot rule out the possibility of a collapse above the deflated reservoir. Occurring after one year, and involving just 1% of the erupted volume, the deforming source ($20 \text{ millions of m}^3$) would be equivalent to a disk of 12 km of diameter subsiding by 0.2 m. Such volume scales with some known sources of tsunami triggered by either earthquakes or landslides. Therefore, appropriate response and preparedness strategy might be implemented for safety in Mayotte and along the surrounding coasts of Madagascar and Africa, including the possible impact on offshore oil and other infrastructures build at shallow depths near the coasts

The ongoing crisis in Mayotte might be important to teach us more about the dynamics of the extension between the Somali plate and the Lwandle block, and the related volcanism. How much of the 2.6 mm yr^{-1} extension is localized along the Comoros volcanic line is unknown. Improving this knowledge and improving the knowledge of the distribution, alignment and ages of the offshore volcanic features, especially around the main islands, may lead to a better understanding of the behaviour, evolution, and related hazard of this peculiar area.

ACKNOWLEDGEMENTS

We are grateful to Jean Battaglia, Julien Bernard, Nicolas Chamot-Rooke, Alison Colombain, Christine Deplus, Andrea Di Muro, Cécile Doubre, Rémi Dretzen, Valérie Ferrazzini, Nathalie Feuillet, Bruno Garayt, Marc Grunberg, Eric Jacques, the Gempa team, the Guralp hotline, Philippe Jousset, Philippe Kowalski, Frédéric Lacquement, Jérôme Lambert, Yohann Legendre, Arnaud Lemarchand, Hélène Lyon-Caen, Estelle Maisonneuve, Aline Peltier, Sébastien Saur, Jean-Marie Saurel, Isabelle Thinon, Jérôme van der Woerd, Pierre Valty for their help and the fruitful discussions. IPGP and ReNaSS performed the observatory work during August 2018. Didier Bertil reprocessed the initial locations and magnitudes. IPGP shared the data from Grande Comores. IGN/RGP and its partners TERIA, Lél@sarl and CNES provided the GNSS data, RESIF-RAP network hosting the YTMZ accelerometer, EDUSISMO for the existence of the station MCHI, ISC for its catalogue of seismicity. The funding was from a BRGM internal project and from French Ministry MTES/DGPR. We used the software GMT to produce maps (Wessel & Smith, 1995), SAC, Seiscomp, GIPSY Oasis 6.4 and bathymetric data from Homonim project (SHOM, 2015) and Gebco_2014 (Weatherall *et al.* 2015). Author contribution statement: D.B. built the monitoring tools, D.B., A.L. and A.R. analyzed the seismological data, P.B. analyzed the GNSS data and made the deformation model, P.B. and A.L. wrote the paper.

REFERENCES

- Ahmed, A., Doubre, C., Leroy, S., Kassim, M., Keir, D., Abayazid, A., Perrot, J., Audin, L., Vergne, J., Nercessian, A., Jacques, E., Khanbari, K., Sholan, J., Rolandone, F. & Al-Gand, I., 2016. Seafloor spreading event in western Gulf of Aden during the November 2010–March 2011 period captured by regional seismic networks: Evidence for diking events and interactions with a nascent transform zone, *Geophysical Journal International*, **205**(2), 1244-1266.
- Audru, J. C., Guennoc, P., Thinon, I. & Abellard, O., 2006. Bathymay: la structure sous-marine de Mayotte révélée par l'imagerie multifaisceaux, *Comptes Rendus Geoscience*, **338**(16), 1240-1249.
- Ayele, A., Jacques, E., Kassim, M., Kidane, T., Omar, A., Tait, S., A. Nercessian, J.-B. de Chabaliér & King, G. (2007). The volcano–seismic crisis in Afar, Ethiopia, starting September 2005. *Earth and Planetary Science Letters*, **255**(1-2), 177-187.
- Bertil, D. & Regnault, J.M., 1998, Seismotectonics of Madagascar, *Tectonophysics*, **294**, 57–74.
- Bertil, D, Roullé, A, Lemoine, A, Colombain, A, Maisonhaute, E & Dectot., G, 2018. MAYEQSwarm2018 : BRGM earthquake catalogue for the Earthquake Swarm located East of Mayotte. May 10th -November 12th 2018, <https://doi.org/10.18144/372c5809-3d30-440c-b44a-1c89385f176a>
- Blewitt, G., Hammond, W.C. & Kreemer, C., 2018. Harnessing the GPS data explosion for interdisciplinary science, *Eos*, **99**, <https://doi.org/10.1029/2018EO104623>.
- Briole, P., De Natale, G., Gaulon, R., Pingue, F. & Scarpa, R., 1986. Inversion of geodetic data and seismicity associated with the Friuli earthquake sequence (1976-1977), *Annales Geophysicae*, **4**(B4), 481-492.
- Briole, P., 2017. Modelling of earthquake slip by inversion of GNSS and InSAR data assuming homogenous elastic medium, *Zenodo*. <http://doi.org/10.5281/zenodo.1098399>
- Calais, E., Ebinger, C., Hartnady, C. & Nocquet, J.M., 2006. Kinematics of the East African Rift from GPS and earthquake slip vector data, *Geological Society, London, Special Publications*, **259**(1), 9-22.
- Daniel, J., Dupont, J. & Jouannic, C., 1972. Relations Madagascar-archipel des Comores (Nord-Est du canal de Mozambique): sur la nature volcanique du Banc du Leven, *Comptes Rendus de l'Académie des Sciences. Série D: Sciences Naturelles*, **274**(12), 1784-1787.
- Davis, J.K., Lawver, L.A., Norton, I.O. & Gahagan, L.M., 2016. New Somali basin magnetic anomalies and a plate Model for the early Indian ocean, *Gondwana research*, **34**, 16–28. <https://doi.org/10.1016/j.gr.2016.02.010>
- Debeuf, D., 2004. Etude de l'évolution volcano-structurale et magmatique de Mayotte, Archipel des Comores, océan Indien: approches structurales, pétrographique, géochimique et géochronologique, PhD, La Réunion University, 277p.
- DeMets, C., Gordon, R.G. & Argus, D.F., 2010. Geologically current plate motions, *Geophysical Journal International*, **181**(1), 1-80.
- Delvaux, D. & Barth, A., 2010. African stress pattern from formal inversion of focal mechanism data, *Tectonophysics*, **482**, 105-128.

- Déprez, A., Doubre, C., Masson, F. & Ulrich, P., 2013. Seismic and aseismic deformation along the East African Rift System from a reanalysis of the GPS velocity field of Africa, *Geophysical Journal International*, **193**(3), 1353-1369.
- Dziewonski, A.M., Chou, T.A. & Woodhouse, J.H., 1981. Determination of earthquake source parameters from waveform data for studies of global and regional seismicity, *J. Geophys. Res.*, **86**, 2825-2852, doi:10.1029/JB086iB04p02825.
- Edusismo, <http://www.edusismo.org>
- Ekström, G., Nettles, M. & Dziewonski, A.M., 2012. The global CMT project 2004-2010: Centroid-moment tensors for 13,017 earthquakes, *Phys. Earth Planet. Inter.*, **200-201**, 1-9, doi:10.1016/j.pepi.2012.04.002.
- Emerick, C.M. & Duncan, R.A., 1982. Age progressive volcanism in the Comores Archipelago, eastern Indian Ocean and implications for Somali plate tectonics, *Earth Planet Sci Lett* **60**(3), 415-428.
- Flower, M. F. J., & Strong, D. F., 1969. The significance of sandstone inclusions in lavas of the Comores Archipelago, *Earth and Planetary Science Letters*, 7(1), 47-50.
- GEOFON Data Centre, 1993. GEOFON Seismic Network. Deutsches GeoForschungsZentrum GFZ. Other/Seismic Network. [doi:10.14470/TR560404](https://doi.org/10.14470/TR560404).
- Gonnermann, H.M. & Manga, M., 2013. Dynamics of magma ascent in the volcanic conduit, in *Modeling Volcanic Processes, The Physics and Mathematics of Volcanism*, eds. Fagents, S.A., Gregg, T.K.P. and Lopes, R.M.C., *Cambridge University Press, Cambridge*.
- Grandin, R., Jacques, E., Necessian, A., Ayele, A., Doubre, C., Socquet, A., Kassim, M., Lemarchand, A. & King, G. C. P. (2011). Seismicity during lateral dike propagation: Insights from new data in the recent Manda Hararo–Dabbahu rifting episode (Afar, Ethiopia). *Geochemistry, Geophysics, Geosystems*, **12**(4).
- Gudmundsson, A., Lecoer, N., Mohajeri N. & Thordarson, T., 2014. Dike emplacement at Bardarbunga, Iceland, induces unusual stress changes, caldera deformation, and earthquakes, *Bull. Volcanol.*, **76**:869, doi:10.1007/s00445-014-0869-8.
- Hainzl, S., 2004. Seismicity patterns of earthquakes swarms due to fluid intrusion and stress triggering, *Geophys. J. Int.*, **159**, 1090-1096, doi:10.1111/j.1365-246X.2004.02463.x
- Horner Johnson, B.C., Gordon, R.G. & Argus, D.F., 2007. Plate kinematic evidence for the existence of a distinct plate between the Nubian and Somalian plates along the Southwest Indian Ridge, *Journal of Geophysical Research: Solid Earth*, **112**(B5).
- International Seismological Centre, 2016. On-line Bulletin, <http://www.isc.ac.uk>, Internatl. Seismol. Cent., Thatcham, United Kingdom, [http://doi.org/10.31905/D808B830](https://doi.org/10.31905/D808B830)
- Kennett, B.L.N., 1991. IASPEI, 1991. Seismological tables, Research School of Earth Sciences, Australian National University.
- Klimke, J., Franke, D., Gaedicke, C., Schreckenberger, B., Schnabel, M., Stollhofen, H., Rose, J. & Chaheire, M., 2016. How to identify oceanic crust—Evidence for a complex break-up in the Mozambique Channel, off East Africa, *Tectonophysics*, **693**, 436-452.

- Klügel, A., Longpré, M.A., García-Cañada, L. & Stix, J., 2015. Deep intrusions, lateral magma transport and related uplift at ocean island volcanoes, *Earth Planet. Sci. Lett.*, **431**, 140-149.
- Lambert, J., 1997. Contribution au relevé de la sismicité historique des îles de la Réunion, de Maurice et des Comores, *BRGM R39736*, 56 p.
- Malod, J.A., Mougenot, D., Raillard, S. & Maillard, A., 1991. Nouvelles contraintes sur la cinématique de Madagascar : les structures de la chaîne de Davie, *C. R. Acad. Sci. Paris*, **312**, Série II, P. 1639-1646.
- Maugé, L.A., Ségoufin, F., Vernier, E. & Froget, C., 1982. Geomorphology and origin of the reef-banks of the North-eastern Mozambique Channel-Western Indian Ocean, *Marine Geology*, **47**, 37-55.
- Michon, L., 2016. The Volcanism of the Comoros Archipelago Integrated at a Regional Scale. In : Active Volcanoes of the Southwest Indian Ocean, Active Volcanoes of the World. P. Bachelery et al (Eds.).
- Mogi, K., 1958. Relations between the eruptions of various volcanoes and the deformations of the ground surfaces around them, *Bull. Earthquake Res. Inst. Univ. Tokyo*, **36**, 99-134.
- Mougenot, D., Recq, M., Virlogeux, P., & Lepvrier, C., 1986. Seaward extension of the East African rift. *Nature*, **321**(6070), 599.
- Nagy, W., 1996. New region-dependent travel-time handling facilities at the IDC; Functionality, testing and implementation details, Tech.Rep. 96/1179, SAIC.
- Nehlig P., Lacquement F., Bernard J., Audru J.-C., Caroff M., Deparis J., Jaouen T., Pelletier A.-A., Perrin J., Prognon C., Vittecoq B., 2013. Notice explicative, carte géol. France (1/30 000), feuille Mayotte (1179). Orléans : BRGM, 74 p. Carte géologique par Lacquement F., Nehlig P., Bernard J., 2013.
- Nougier, J., Cantagrel, J.M., & Karche, J.P., 1986. The Comores archipelago in the western Indian Ocean: volcanology, geochronology and geodynamic setting, *Journal of African Earth Sciences* (1983), **5**(2), 135-144.
- Okada, Y., 1992. Internal deformation due to shear and tensile faults in a half space, *Bull. Seism. Soc. America*, **82**, 1018–1040.
- Pelleter, A.A., Caroff, M., Cordier, C., Bachèlery, P., Nehlig, P., Debeuf, D., & Arnaud, N., 2014. Melilite-bearing lavas in Mayotte (France): An insight into the mantle source below the Comores, *Lithos*, **208**, 281-297.
- Rabinowitz, P. D., Coffin, M. F. & Falvey, D., 1983. The separation of Madagascar and Africa. *Science*, **220**(4592), 67-69.
- Roland, E. & Mc Guire, J.J., 2009. Earthquake swarms on transform faults, *Geophys. J. Int.*, **178**, 1677-1690, doi: 10.1111/j.1365-246X.2009.04214.x
- Saria, E., Calais, E., Stamps, D.S., Delvaux, S. & Hartnady, C.J.H., 2014. Present-day kinematics of the East African Rift, *J. Geophys. Res. Solid Earth*, **119**, doi:10.1002/2013JB010901.
- Scripps Institution of Oceanography, 1986. IRIS/IDA Seismic Network. International Federation of Digital Seismograph Networks. Other/Seismic Network. doi.org/10.7914/SN/II

- Ségoufin, J., 1981. Morphologie et structure du Canal de Mozambique, PhD, Univ. Strasbourg, France, 236p.
- Ségoufin, J. & Patriat, P., 1981. Reconstructions of the western Indian Ocean at anomalies M21, M2 and 34 times. Madagascar paleoposition, *Bull. Soc. Géol. France*, **6**, 603-607.
- SHOM, 2015. MNT Bathymétrie de façade Atlantique (Projet Homonim). http://dx.doi.org/10.17183/MNT_ATL100m_HOMONIM_WGS84
- Shuler, A., Ekström, G., & Nettles, M., 2013. Physical mechanisms for vertical-CLVD earthquakes at active volcanoes, *Journal of Geophysical Research: Solid Earth*, **118**(4), 1569-1586.
- SISFRANCE-Océan Indien, 2010. BRGM <http://www.sisfrance.net/Reunion/index.asp>
- Stamps, D. S., Saria, E. & Kreemer, C., 2018. Geodetic Strain Rate Model for the East African Rift System, *Scientific reports*, **8**(1), 732.
- Toda, S., Stein, R.S. & Sagiya, T., 2002. Evidence from the AD 2000 Izu islands earthquake swarm that stressing rate governs seismicity, *Nature*, **419**(6902), 58.
- Weatherall, P., Marks, K. M., Jakobsson, M., Schmitt, T., Tani, S., Arndt, J. E., Rovere, M., Chayes, D., Ferrini, V. & Wigley, R. (2015). A new digital bathymetric model of the world's oceans. *Earth and Space Science*, **2**(8), 331-345.
- Weichert, D.H., 1980. Estimation of the earthquake recurrence parameters for unequal observation periods for different magnitudes, *Bulletin of the Seismological Society of America*, **70**(4), 1337-1346.
- Wessel, P. & Smith, W.H.F., 1995. New version of the generic mapping tools released, *EOS, Trans. Am. geophys. Un.*, **76**, 329.
- Yukutake, Y., Ito, H., Honda, R., Harada, M., Tanada, T. & Yoshida, A., 2011. Fluid induced swarm earthquake sequence revealed by precisely determined hypocenters and focal mechanisms in the 2009 activity at Hakone volcano, Japan, *Journal of Geophysical Research: Solid Earth*, **116**(B4).
- Zinke, J., Reijmer, J.J.G., Thomassin, B.A., Dullo, W.C., Grootes, P.M. & Erlenkeuser, H., 2003a. Postglacial flooding history of Mayotte lagoon (Comoro archipelago, southwest Indian Ocean), *Marine Geology*, **194**(3-4), 181-196.
- Zinke, J., Reijmer, J.J.G. & Thomassin, B.A., 2003b. Systems tracts sedimentology in the lagoon of Mayotte associated with the Holocene transgression, *Sedimentary Geology*, **160**(1-3), 57-79.

APPENDICES

Site		Long	Lat	v_E	v_N	σ_E	σ_N	r_E	r_N
		°	°	Mm/yr	mm/yr	mm/yr	mm/yr	mm/yr	mm/yr
ABPO	Madagascar	47.229	-19.018	18.5	14.0	0.2	0.2	-1.2	-0.1
ARSH	Tanzania	36.698	-3.387	24.5	17.5	0.3	0.3	-0.8	-0.4
ASOS	Ethiopia	34.553	10.051	22.9	17.9	0.2	0.2	-7.3	-0.8
DODM	Tanzania	35.748	-6.186	22.2	18.0	0.3	0.3	-2.1	-0.3
EBBE	Uganda	32.445	0.038	24.9	16.3	0.2	0.2	-1.7	-3.1
ERAS	South Africa	27.696	-23.687	18.2	18.2	0.2	0.2	0.2	-3.0
FG04	Uganda	32.587	0.313	24.0	16.5	0.4	0.3	-2.7	-2.9
GETA	Tanzania	32.217	-2.881	24.6	18.7	0.4	0.4	-0.9	-0.8
INHB	Mozambique	35.383	-23.871	18.5	17.9	0.4	0.4	0.5	-0.5
KASM	Zambia	31.225	-10.172	20.5	18.1	0.2	0.2	-2.4	-1.8
LLNG	Malawi	33.789	-13.947	19.6	17.4	0.3	0.3	-1.9	-1.6
MAL2	Kenya	40.194	-2.996	26.5	15.8	0.2	0.2	1.0	-0.9
MAYG	Mayotte	45.258	-12.782	21.9	14.8	0.2	0.2	0.0	0.0
METU	Ethiopia	35.586	8.271	23.2	17.8	0.3	0.3	-6.3	-0.5
MOIU	Kenya	35.290	0.288	24.4	18.3	0.2	0.2	-2.3	-0.1
MPIK	Zambia	31.451	-11.821	20.4	18.1	0.3	0.3	-1.9	-1.7
MTVE	Tanzania	40.166	-10.260	23.2	15.7	0.2	0.2	0.3	-1.0
NEGE	Ethiopia	39.589	5.335	28.0	17.3	0.2	0.2	-0.5	0.4
NMPL	Mozambique	39.258	-15.123	20.0	16.2	0.4	0.4	-1.1	-0.8
PANO	Réunion	55.687	-21.002	16.2	12.8	0.3	0.3	-2.8	1.7
PBWA	South Africa	31.134	-23.952	17.8	17.8	0.2	0.2	-0.1	-2.1
PMBA	Mozambique	40.484	-12.964	20.5	15.9	0.4	0.4	-1.4	-0.7
RCMN	Kenya	36.893	-1.221	26.4	17.0	0.2	0.2	0.3	-0.8
RDRG	Rodrigues	63.426	-19.681	17.2	8.8	0.3	0.3	-2.3	0.5
SEYG	Seychelles	55.531	-4.679	25.6	12.0	0.2	0.2	0.7	0.9
SLEU	Réunion	55.572	-21.208	16.4	12.4	0.2	0.2	-2.5	1.3
TANZ	Tanzania	39.208	-6.766	22.2	17.0	0.2	0.2	-1.9	0.0
TDOU	South Africa	30.384	-23.080	17.9	17.7	0.2	0.2	-0.3	-2.5
TETE	Mozambique	33.576	-16.147	19.0	17.7	0.3	0.3	-1.7	-1.3
TEZI	Zambia	26.016	-15.747	19.4	18.8	0.2	0.2	-1.5	-3.0
TNDC	Tanzania	37.341	-11.063	22.2	16.9	0.2	0.2	-0.4	-0.8
ULUB	DRC	27.485	-11.631	23.3	19.5	0.3	0.3	0.9	-1.7
VACS	Mauricius	57.497	-20.297	17.0	11.0	0.2	0.2	-2.2	0.6
VHMR	Madagascar	49.921	-13.458	21.6	14.6	0.5	0.5	-0.1	1.4
VOIM	Madagascar	46.793	-21.906	18.2	14.4	0.3	0.3	-0.5	0.1
ZAMB	Zambia	28.311	-15.426	20.3	18.2	0.2	0.2	-0.7	-2.7
ZBMT	Madagascar	44.733	-22.827	17.0	15.2	0.5	0.5	-1.3	0.2

Appendix 1. ITRF2014 horizontal velocity of GNSS stations around Mayotte. The time series are from the Nevada geodetic laboratory (Blewitt *et al.* 2018). The two right columns contain the

relative velocities after cancelling the global rotation by applying a clockwise rotation equivalent to $2.1^\circ \text{ Myr}^{-1}$, and setting zero motion in MAYG.

Code	Lat	Long	Type of sensor (network)	Location	Implementation
YTMZ	-12.7557	45.2307	Accelerometer (RAP)	Mamoudzou (Mayotte)	continuous
ABPO	-19.0183	47.2292	BB (IRIS/IDA)	Ambohipanombo (Madagascar)	continuous
VOI	-21.9065	46.7933	BB (GEOFON)	Vohitsoka (Madagascar)	continuous
KIBK	-2.3591	38.0433	BB (GEOFON)	Kibwezi (Kenya)	continuous
SBC	-11.6491	43.2969	BB (Karthala observatory)	Grande Comore	05/30 ⁻
CAB	-11.7486	43.3435	BB (Karthala observatory)	Grande Comore	05/30 ⁻
MOIN	-11.7659	43.2435	BB (Karthala observatory)	Grande Comore	05/30-08/6
MCHI	-12.8329	45.1237	BB (Edusismo)	Chiconi (Mayotte)	06/27 ⁻
RCBF0	-12.7984	45.2748	Raspberry shake 3D	Pamandzi (Mayotte)	06/26-07/10
RAE55	-12.7335	45.2036	Raspberry shake 1D	Koungou (Mayotte)	06/26 ⁻
SBV	-13.4584	49.9212	BB (GEOFON)	Sambava (Madagascar)	07/15 ⁻

Appendix 2. The eleven stations of the Mayotte virtual seismic network. BB means broadband.

Date	Location			Magnitude		Moment	Plane 1			Plane 2		
	Long	Lat	depth	m_l	M_w	$\times 10^{16}$	Strike	Dip	Rake	Strike	Dip	Rake
	$^\circ\text{E}$	$^\circ\text{S}$	km			N m	$^\circ$	$^\circ$	$^\circ$	$^\circ$	$^\circ$	$^\circ$
14/05 14:41	45.69	12.70	36	5.1	5.2	7.2	354	62	4.0	262	87	152
15/05 15:48	45.71	12.72	34	5.8	5.9	82.8	347	61	-8	81	83	-151
20/05 08:01	45.66	12.76	36	5.0	5.4	17.6	346	47	-4	79	87	-137
21/05 00:47	45.69	12.73	38	5.1	5.5	23.4	351	53	-1	82	89	-143
22/05 12:37	45.70	12.75	41	5.0	5.0	4.7	330	41	16	227	79	130
25/05 05:43	45.68	12.74		5.1								
25/05 06:36	45.68	12.76	31	5.4	5.1	6.2	350	73	8	258	82	162
26/05 00:32	45.69	12.75	39	5.3	4.9	2.9	341	68	11	247	80	158
28/05 22:12	45.75	12.72		5.1								
30/05 05:54	45.71	12.75	32	5.5	5.1	5.2	354	69	3	263	87	159
30/05 16:21	45.72	12.73		5.1								
01/06 03:24	45.72	12.72		5.3								
01/06 03:35	45.72	12.74		5.3								
01/06 05:44	45.72	12.74		5.2								
01/06 07:14	45.70	12.74	42	5.0	5.0	3.4	355	76	7	263	83	166
01/06 08:28	45.72	12.74		5.0								
02/06 07:42	45.72	12.74		5.2								
02/06 17:39	45.72	12.72		5.1								

THE VOLCANO-TECTONIC CRISIS OF 2018 EAST OF MAYOTTE, COMORO ISLANDS

03/06 06:13	45.72	12.74	30	5.2	5.1	6.4	350	68	-9	83	81	-158
04/06 18:51	45.73	12.69		5.1								
04/06 19:53	45.71	12.75	31	5.4	5.0	4.6	352	73	7.0	260	83	163
04/06 21:20	45.73	12.76	22	5.4	5.0	4.5	1	68	-2	92	89	-158
05/06 23:02	45.71	12.77	25	5.0	5.1	4.8	347	58	1	257	89	148
06/06 09:37	45.72	12.76	22	5.0	4.9	3.3	345	67	11	250	80	156
08/06 12:03	45.71	12.71	15	5.0	4.9	3.0	247	62	153	350	67	31
12/06 17:17	45.75	12.77	12	5.4	5.4	15.7	4	58	8	269	83	148
23/06 19:45	45.73	12.72	12	5.0	5.0	4.2	360	60	7	267	84	149
25/06 17:41	45.80	12.73	12	5.0	5.3	10.8	1	57	9	266	82	147
27/06 06:40	45.75	12.73	19	5.0	5.2	8.7	1	70	14	267	77	159

Appendice 3. The 29 events with $m_l \geq 5.0$, all occurring during the first 50 days of the crisis between 2018 May 15 and June 27. For 20 of them there is an available G-CMT, with the fault planes 1 and 2 reported.